
Experimental Investigation of Acoustic Noise in Ultrasound RFTS-Based Tissue Classification

By

KEVIN MULTANI
CONRAD NG
KEVIN SHEN



Engineering Physics 459
Department of Engineering Physics
UNIVERSITY OF BRITISH COLUMBIA

APRIL 4, 2016

PROJECT NUMBER: 1608

EXECUTIVE SUMMARY

The primary objective of this investigation of acoustic noise in ultrasound RFTS-based tissue classification is to determine whether microvibrations caused by external forces, such as noise, are captured by the ultrasound sound response as a source of information to aid classification. The experiments conducted were designed to explore this area of interest, as well as to gain insight into the physical mechanisms of how different media interact uniquely with ultrasound signals.

The experiments were divided into two major categories; namely, experiments without induced noise, and experiments with induced noise. The induced noise was provided by an external speaker emitting a low frequency at a constant amplitude. All experiments were done on and off an optical table to isolate the effect of ambient noise. The collected data was then run through a Fourier feature extraction analysis, data cleansing to eliminate anomalous data sets, and classification using a support vector machine (SVM) machine learning algorithm. χ^2 -tests were conducted to test the quality of the classification results, and various methods such as SVM parameter grid searches were performed to optimize the SVM classification. Physical theories relating the power spectrum from the Fourier transform to the tissue type under examination were presented. The features used in the SVM classification were theoretically shown to depend more on tissue scatterer or cell size rather than tissue elasticity, and therefore perform more accurate classification on tissues with different cell sizes.

The primary results drawn from the experiments were that there was no significant change in classification accuracy on and off the optical table. Altering the ultrasound probe frequency and power also had little effect on the classification accuracy. We concluded that microvibrations from external sources are not a reliable source of information. An important consequence of our experimental analysis was that we found that scatterer phantoms consistently classified better than the elasticity phantoms. This result confirms the theory that the Fourier transform features used in the SVM classification are more dependent on scatterer size than elastic moduli.

Moving forward, our primary recommendation based on results from this investigation would be to experiment with new features to use in classification. The set of features currently used in the SVM model are dependent on the scatterer sizes of the sample, but to classify between tissues with various elastic properties, different features may be required. A suggestion would be features more related to absorption than frequency.

TABLE OF CONTENTS

	Page
List of Tables	iv
List of Figures	v
1 Introduction	1
1.1 Motivation	1
1.2 Previous Microvibration Results	2
1.3 Project Objectives	4
1.4 Background	5
1.4.1 Interaction with Tissue	5
1.4.2 Time Series Analysis	8
1.4.3 Mechanical Properties: Healthy and Cancerous Tissue	8
1.5 Scope and Limitations of Project	11
2 Experimental Procedure	13
2.1 Ultrasound Equipment	13
2.1.1 Analogic SonixTouch Ultrasound System	13
2.1.2 L14-5/38 Linear Transducer	15
2.1.3 Philips Phantoms	15
2.2 Experiments without Induced Noise	17
2.3 Experiments with Induced Noise	19
2.4 Experiment Set I	20
2.5 Experiment Set II	22
3 Analysis, Results, and Discussion	24
3.1 Feature Extraction	24
3.1.1 Regions of Interest (ROIs)	25
3.1.2 Fast Fourier Transform	25
3.1.3 Features 1 – 4: Frequency Domain Quadrants	25
3.1.4 Features 5 & 6: Linear Fit to Fourier	27

TABLE OF CONTENTS

3.1.5 Feature 7: Fractal Dimension	27
3.1.6 Feature 8: Spectrum Dot Product	28
3.1.7 Feature 9: Daubenchies Wavelets	28
3.2 Data Cleansing	28
3.3 Tissue Classification with a SVM	30
3.3.1 SVM Code Library	30
3.4 Results	31
3.4.1 Classification Results: Data Set I	31
3.4.2 Classification Results: Data Set II	34
3.4.3 Test of Significance	37
3.4.4 Different Kernels of the SVM	38
3.4.5 SVM Parameter Grid Search	40
3.4.6 Feature Dropout Analysis	41
3.4.7 Feature Visualization	43
3.4.8 Physical Model and Validation	46
4 Denouement	50
4.1 Experimental Limitations	50
4.2 Conclusions	52
5 Project Deliverables	54
5.1 List of Deliverables	54
5.2 Financial Summary	54
5.3 Ongoing Commitments	55
6 Recommendations	56
Bibliography	58

LIST OF TABLES

TABLE	Page
1.1 Previous Microvibration Experiment Parameters	3
1.2 Results of Previous Microvibration Experiments	4
2.1 Uniform Elasticity Phantom Specifications	16
2.2 Uniform Scatterer Phantom Specifications	17
2.3 Experiment Set I without Induced Noise	21
2.4 Experiment Set I with Induced Noise	21
2.5 Experiment Set II: Varying Frequency and Power	23
3.1 Experiment Set I: Elasticity Experiments Legend	33
3.2 Experiment Set I: Scatterer Experiments Legend	33
3.3 Experiment Set II: Elasticity Experiments Legend	34
3.4 Experiment Set II: Scatterer Experiments Legend	34

LIST OF FIGURES

FIGURE	Page
1.1 RF Time series example	3
1.2 The different types of interaction	5
1.3 RF Time series example	9
1.4 Elastic Moduli of Benign vs Cancerous tissue	10
2.1 SonixTouch Ultrasonix Ultrasound Machine	14
2.2 L14-5/38 Linear Transducer	15
2.3 Uniform Elasticity Phantom	16
2.4 Uniform Scatterer Phantom	17
2.5 Newport Electronic Vibration Isolation System (Optical Table)	18
2.6 Experiments with No Noise Block Diagram	18
2.7 Undamped Experiment without Induced Noise	19
2.8 Damped Experiment without Induced Noise	19
2.9 Experiments with Noise Block Diagram	20
2.10 Undamped Experiment with Induced Noise	22
2.11 Damped Experiment with Induced Noise	22
3.1 Data Analysis Flowchart	24
3.2 Anomalous Noise Displacement in Collected Data	29
3.3 Indicator Signal Plot for Identifying Anomalous Noise	30
3.4 Experiment Set I: Classification Accuracy	32
3.5 Experiment Set II: 10.0 MHz Classification Accuracy	35
3.6 Experiment Set II: 6.6 MHz Classification Accuracy	36
3.7 χ^2 -Test of Significance	37
3.8 Gaussian Kernel in 1-D Feature Space	38
3.9 Linear and Polynomial Kernels	39
3.10 Classification Accuracy of Elasticity Phantoms with Different Kernels	39
3.11 Classification Accuracy of Scatterer Phantoms with Different Kernels	40
3.12 Classification Accuracy with Dropout for Scatterer Phantom	42
3.13 Classification Accuracy with 1 Feature for Scatterer Phantom	42

LIST OF FIGURES

3.14 Classification Accuracy with Dropout for Elasticity Phantom	43
3.15 Classification Accuracy with 1 Feature for Elasticity Phantom	44
3.16 Visualization One	45
3.17 Visualization Two	46
3.18 Visualization Three	47

INTRODUCTION

This chapter outlines introductory information about the project. The primary motivation of this project is to contribute to the research of our project sponsor, Dr. Purang Abolmaesumi, his team, and Philips Research North America in the development of a new Ultrasound based Prostate Cancer detection Technique. Firstly, we will discuss the motivation and significance of the project. Previous results will be presented to provide context for the following project objectives. Then, background information will be described which focuses on concepts used in the analysis, experimentation, and discussion. Lastly, the scope and limitations of this project will be stated.

Following Chapter 1, the chapters in this report will first detail the various experimental procedures performed and their particular set-ups. The analysis methods and machine learning classification on the gathered RF data will then be described with results presented and connected to physical theories. Then, the conclusions and project deliverables drawn from the results will be discussed and summarized. Finally, recommendations for future investigations and an addendum of data analysis code will be appended to the end of the report.

1.1 Motivation

Prostate Cancer is the most common cancer among Canadian men. It is the third leading cause of death from cancer in men in Canada. According to the Canadian Cancer Society, it is estimated that 24,000 (representing 24% of new cancer cases) men will be diagnosed with prostate cancer, of which 4,100 will die. These numbers, however, are likely to double by 2025, when the baby boomer generation will reach the age of peak prevalence. If the diagnosis is prompt, the

five-year survival rate can be over 95% [www.cancer.ca].

Early diagnosis and accurate staging of prostate cancer enables treatment options that cater to the patient: surgery, ablation, and radiation therapy are some examples [4, 6]. Common diagnosis procedures of prostate cancer include a Digital Rectal Examination (DRE), a palpitory examination of the prostate, and/or the measurement of the Prostate Specific Antigen (PSA). However, these methods are not definitive. DRE is effective for finding small tumors and PSA changes can be non-cancer related, such as the enlargement of the prostate with age [15]. Currently, the most reliable diagnosis method is a core-needle biopsy under the guidance of transrectal ultrasound (TRUS) [9]. The biopsy involves taking tissue samples from predefined anatomical regions of the prostate, which means the procedure is performed blind. Conventional ultrasound imaging is not capable of differentiating cancerous and normal tissue regions with high sensitivity and specificity. New techniques have been proposed to enable a targeted biopsy by extracting tissue-type information from the ultrasound signal, in hopes of improving prostate cancer detection rate [12].

Machine Learning (ML) methods that use ultrasound data for prostate cancer detection utilize features extracted from radio frequency (RF) and B-mode ultrasound images are beginning to be utilized. Features from both B-mode images and calibrated spectrum of a single RF frame have been used to classify prostate cancer [7, 8, 17]. The major limitation of B-mode imaging is a loss of information due to post-processing of the signal, whereas analysis of single-RF-frame-spectrum suffers from the lack of a standard method of calibration [21]. Recently, a novel technique has been used for classification in a machine learning framework. A sequence of ultrasound RF frames is captured in time from a stationary tissue location (hereafter referred to as *RF time series* or *RFTS*) produces features for the machine learning [5, 11, 17, 18]. This RFTS method outperforms other ML techniques [18].

The project proposed by this report will investigate the physical mechanisms of the RFTS method, which was developed by our sponsor, Dr. Purang Abolmaesumi and his team [5, 11, 17, 18].

1.2 Previous Microvibration Results

The following section describes the previous work targeting the microvibration hypothesis. After a brief summary of its methods, the conclusions from this investigation will be discussed.

A previous study on the microvibration hypothesis showed that tissue classification performs worse in the absence of vibration sources in the environment. The RFTS method was used to

classify different phantoms (varying scatterer sizes and elasticities), first on a regular table, then on an *optical* table, where external vibration is minimized (see Table 1.1) (under constant ultrasound settings).

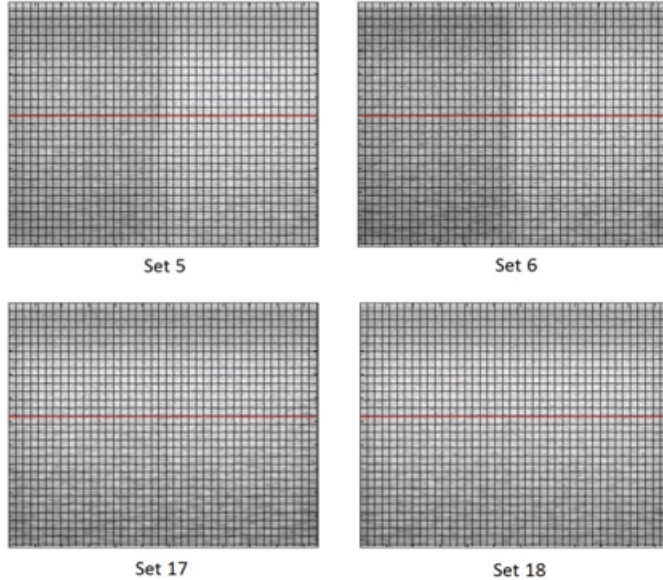


Figure 1.1: This figure shows the post-processed (applied Hilbert transform, then log-compressed) B-mode ultrasound images of four different phantoms. For an arbitrary data set, the left and the right side have different properties (Table 1.1). The machine learning takes each half and divides it into two sets, the training set and the testing set. Results are the performance of the trained classifier on the testing set, summarized in Table 1.2.

The results shown in Table 1.2 show that both the classification accuracy and discrimination power are much greater when the image is not taken on an optical table. Hence, it was inferred that tissue vibrations caused by acoustic effects and the environment around the setup changes the backscattering of ultrasound, and enhances classification.

Experiments				
	Set 5	Set 6	Set 17	Set 18
Phantom	Scatterer		Uniform Elasticity	
Description	Left: 30-50 micron		Left: 34 kPa	
	Right: 7-10 micron		Right: 15.9 kPa	
Table	Optical	Regular	Optical	Regular

Table 1.1: This table shows the description of each situation in the previous microvibration experiment. Each set corresponds to the B-mode images in Figure 1.1. For each set, the phantom consists of two physically different properties (left and right – corresponds to left and right in the figure) and the machine learning is meant to classify the left and right side.

Results				
	Set 5	Set 6	Set 17	Set 18
Classification Accuracy	78%	98%	54%	94%
AUC	0.82	1.00	0.48	0.98
Table	Optical	Regular	Optical	Regular

Table 1.2: This table shows the results from the machine learning.

The study concluded that there must be further investigation into this effect and hypothesis that microvibrations in the surroundings improve tissue classification accuracy.

1.3 Project Objectives

While extensive studies have shown the effectiveness of classification using RFTS methods, less is known about why the variations even exist in the RF time series data . In the situation of RFTS, everything is held stationary in space. When taking ultrasound images from frame to frame, it is expected that the signal characteristics remain constant. However, this is not the case due to acoustic noise perturbations. The aim of the project is to connect the effect of noise in this time series analysis and connect physical meaning to the results. Hereafter the time series variations will be referred to as sources of *information*.

Previous work has identified a hypothesis, detailed below, that suggests how sources of information aid in the classification between tissue types. Although the previous works have identified possible sources of information, their results are not decisive. The experiments and analysis described in this report will address this issue directly and provide a connection between the results and physical relationships.

Hypothesis:

Microvibrations in the tissue caused by acoustic radiation force and environmental factors, are captured by the RFTS as a source of information.

This project has been catered around investigating this primary idea. However, in our investigations, we uncover the limitations of the ultrasound classification techniques and gain insight into the physical mechanisms by which various media interact differently with ultrasound signals. Much of why temporal ultrasound is successful and a discussion of feature selection for classification has been lacking in literature. Most groups tend to do classification with different sets of features without a thorough investigation of the motivation for selecting the features based on physical grounds. In this analysis, we present our own theories about the physics that allows Machine Learning techniques to differentiate tissue samples and make recommendations

for future work based on our theoretical model.

1.4 Background

1.4.1 Interaction with Tissue

There are different ways that ultrasound can interact with tissue. Figure 1.2 outlines the different modes of interaction: attenuation, absorption, reflection, scattering, refraction and diffraction.

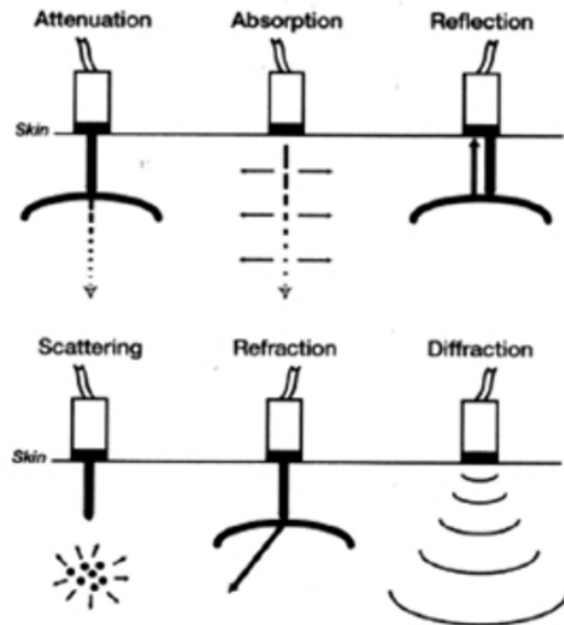


Figure 1.2: The different modes of interaction of ultrasound with tissue. Image courtesy of <http://www.criticalecho.com/content/tutorial-1-basic-physics-ultrasound-and-doppler-phenomenon#>.

1.4.1.1 Attenuation

Attenuation is the term used to account for loss of amplitude (signal). In the context of this project, most of the attenuation is accounted by the remaining interaction modes: absorption, reflection, scattering, refraction, and diffraction. Because attenuation is a conglomerate of other phenomenon, its model is complex; it agrees well with experiments, but the theory cannot be formulated easily. Experiments suggest the amplitude decay model,

$$A(z) = A_0 e^{-\mu_A z}. \quad (1.1)$$

μ_A is called the amplitude attenuation factor and has units of inverse length. Since $20 \log_{10}(\frac{A(z)}{A_0})$ is the amplitude drop in decibels, it is useful to define the attenuation coefficient α as,

$$\alpha = 20 \log_{10}(e) \mu_A \approx 8.7 \mu_A. \quad (1.2)$$

It is useful to think of α as a key parameter carrying all of the attenuation information. Often, the approximation $\alpha(f) \approx af$ is used in practice and so the following attenuation model results,

$$A(z, f) = A_0 e^{-\alpha(f)z/8.7}. \quad (1.3)$$

Since the reflection time is a function of depth (z), one expects a weaker signal (stronger attenuation) as time progresses. This weaker signal is not necessarily less has reflected, but because there is less signal *to be* reflected. This time-dependent attenuation causes severe signal loss and image distortion, if not compensated. All ultrasound systems are equipped with Time Gain Compensation (TGC) circuitry – a time-varying amplification mechanism.

1.4.1.2 Absorption

Absorption in soft tissue like skin, fat, tendons, ligaments, etc. accounts for 80% of ultrasound attenuation [<http://usra.ca/tissue.php>]. Absorption is the conversion of acoustic energy into thermal energy as the ultrasound waves propagate through the medium. Three main factors affect absorption: viscosity of the medium, relaxation time of the medium and the ultrasound frequency [19]. Increasing viscosity increases absorption. Relaxation time is proportional to the time taken by the medium particles to revert back to original mean positions following displacement by an ultrasound pulse. The longer the relaxation time of the medium, the higher the absorption [19]. Lastly, absorption increases with increasing frequency.

1.4.1.3 Reflection

When a beam of ultrasound strikes the boundary between two media, it is partly transmitted and partly reflected. The reflected wave is called an echo and the production and detection of echoes form the basis of ultrasound. There are two types of reflection: specular and non-specular. Specular reflection occurs when the medium boundary is smooth and large relative to the beam. Non-specular reflection (also known as scattering) occurs when the boundary is irregular and small relative to the beam.

Reflection is considered specular when the diameter of the reflector is greater than the wavelength of the ultrasound beam. Models of specular reflection are simple,

$$\text{Specular reflection} \Leftrightarrow \text{Angle of incidence} = \text{Angle of reflection} \quad (1.4)$$

The amount of reflection that occurs at the boundary depends on the acoustic impedance of the two media,

$$Z = \rho v = \rho \frac{1}{\sqrt{\rho \kappa}} = \sqrt{\frac{\rho}{\kappa}}. \quad (1.5)$$

ρ is the density of the medium, v is the speed of sound in the medium, κ is the compressibility of the medium [19]. If the difference in acoustic impedance between the two media is small, a weak echo will be produced, and most of the ultrasound will carry on through the second medium. If the difference in acoustic impedance is large, a strong echo will be produced. This is seen in equation 1.6, which models the simple case where a beam strikes the reflector normal to its boundary.

$$\frac{I_{reflect}}{I_{incident}} = \frac{(Z_1 - Z_2)^2}{(Z_1 + Z_2)^2}. \quad (1.6)$$

$I_{incident}$ is the incident beam's intensity and $I_{reflect}$ is the reflected beam's intensity. Typically in soft tissues, the amplitude of an echo produced at a boundary is only a small percentage of the incident amplitudes.

1.4.1.4 Scattering

Reflection is non-specular when the reflecting interface is irregular, and its size is small relative to the diameter of the ultrasound beam. Non-specular reflection (scattering) is difficult to model theoretically because the incident beam is reflected in many different directions. This reflection is a function of the sizes of the scattering target and the ultrasound beam diameter. When the dimension of the structures on an interface becomes about one wavelength of the ultrasound beam, we enter the scattering regime. Typical wavelengths for diagnostic ultrasound beams is about 1mm. This is within the order of magnitude of micro-structures on an organ, hence making scattering a useful source of information for ultrasound imaging. Scattering shows very strong frequency dependence, increasing rapidly as the frequency of ultrasound is increased [19].

1.4.1.5 Refraction

Refraction is a change in beam direction at a boundary between two media in which ultrasound travels at different velocities (V_1 and V_2). The change in velocity is caused by the change in wavelength as the ultrasound crosses from the first medium to the second while the frequency remains constant. The relationship between the angle of incidence and the angle of refraction is governed by Snell's law as in optics:

$$\frac{\sin(\theta_i)}{\sin(\theta_r)} = \frac{V_1}{V_2}. \quad (1.7)$$

1.4.1.6 Diffraction

Diffraction of an ultrasound beam describes the spreading out of beam energy as it moves away from the source. Diffraction affects the intensity of the beam both axially and laterally.

In diagnostic ultrasound, the dimensions of the ultrasound beam, and the manner in which it diffracts, has great influence on image resolution and imaging depths.

Diffraction determines the ultrasound beam shape. Typically, the ultrasound beam spreads out as it moves away from the transducer. In the *near field* regime or *Fresnel zone*, the beam is still narrow and has a diameter not much bigger than the piezoelectric crystal source. After a certain distance, the beam enters the *far field* regime, or *Fraunhofer zone* where it begins to diverge and diffract to a bigger diameter. This results in a degradation of spatial resolution of the image [20].

The **focus** of a transducer is the point on the central beam axis which is equidistant from all points on the surface of the transducer. For all linear paths between the focus and the surface of the transducer, the times of flight are equal. Areas within the beam close to the focus will have properties which will closely match those at the focus itself. This region around the focus is called the **focal zone** of the transducer. In the context of diagnostic ultrasound, it is ideal to have a well focused beam in the region of interest, in order to get an optimal quality image [20].

1.4.2 Time Series Analysis

The RFTS technique uses ultrasound time series data obtained from a stationary location of tissue, to characterize between various tissue types (Fig. 1.3). This approach has been effective at both high frequency (20–60 MHz) and clinical frequencies (2–10 MHz) [18]. After collecting the ultrasound data and some post-processing (envelope detection and log-compression), the data is sent to a Machine Learning framework – an SVM classifier. Within the framework, some features are constructed, such as: intercept and slope of the fitted regression line to the data, spectral properties, and fractal dimension. After the features are constructed, training, and validation occur before making classifications of other RFTS data.

The machine learning framework will be used heavily in this project. It will be used to quantitatively compare different experiments. The single, most important metric that will be used is the classification accuracy – how well can the machine learning distinguish between tissues. We will test various scenarios, such as: how the feature value changes with respect to the experimental variable (microvibrations, temperature, jitter, or other), how the accuracy changes in different conditions, how does stiffness between tissue types play a role, and any other permutation we can conceive.

1.4.3 Mechanical Properties: Healthy and Cancerous Tissue

The following section serves to provide ample background knowledge to critically think about the designed experiments and interpret results. We are motivated to investigate the effect microvibrations on ultrasound response of the medium by the fact that there are known mechanical differences between healthy and cancerous tissue.

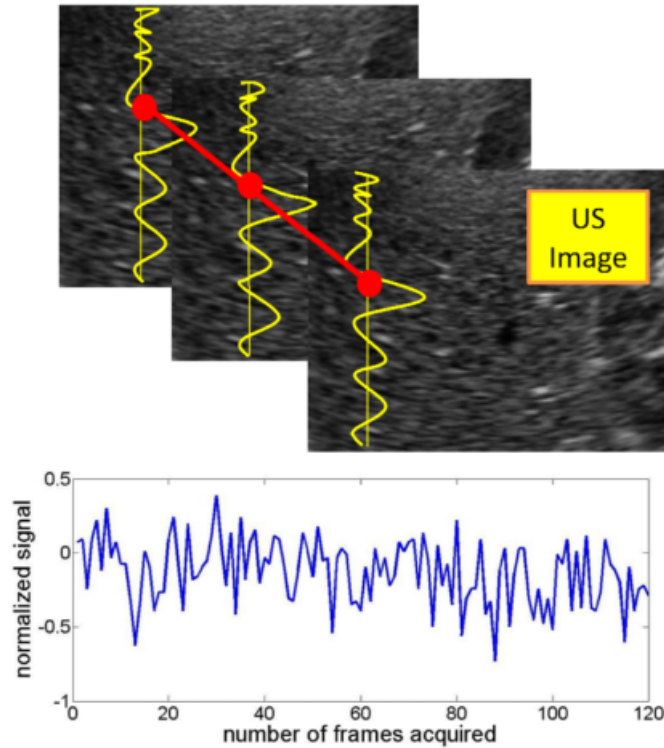


Figure 1.3: This figure shows how the RF time series signal is captured. The top part of the figure shows different frames of the same position being measured, whereas the bottom part shows a sample data set plotted against time (frame number). Image courtesy of [10].

1.4.3.1 Viscoelastic Theory

In order to understand these differences, we can model tissue as a viscoelastic material, one which shows both elastic and viscous mechanical behavior. A purely elastic material responds to an oscillatory stress (Eq. 1.8) linearly (Eq. 1.9) where $\epsilon(t)$ is the time-dependent strain. On the other hand, for a perfectly viscous material, the stress is related to the rate of change of the strain (Eq. 1.10). We note that a sine wave is a $\frac{\pi}{2}$ shifted cosine and that the viscous response is simply a phase-lagged variant of the elastic response.

$$\sigma(t) = \sigma_0 \cos \omega t \quad (1.8)$$

$$E(t) = \frac{\sigma}{\epsilon} = c \Rightarrow \epsilon(t) = \epsilon_0 \cos \omega t \quad (1.9)$$

$$\epsilon(t) = \epsilon_0 \sin(\omega t) = A \cos(\omega t - \frac{\pi}{2}) \quad (1.10)$$

A viscoelastic material will show some intermediate behavior between purely elastic and purely viscous. It will have a strain response of,

$$\epsilon(t) = A \cos(\omega t - \delta). \quad (1.11)$$

δ is a phase-lag between 0 (purely elastic) and $\frac{\pi}{2}$ (purely viscous). If the system is analyzed in the complex domain, one can define a complex Young's Modulus (Eq. 1.12) and corresponding elastic modulus (Eq. 1.13) and viscous modulus (Eq. 1.14):

$$E^* = \frac{\sigma^*}{\epsilon^*} = \frac{\sigma_0 \cos(\omega t) + i\sigma_0 \sin(\omega t)}{\epsilon_0 \cos(\omega t - \delta) + i\epsilon_0 \sin(\omega t - \delta)} = \frac{\sigma_0}{\epsilon_0} e^{i\delta}, \quad (1.12)$$

$$E_{elastic} = \text{Re}[E^*] = \frac{\sigma_0}{\epsilon_0} \cos(\delta), \quad (1.13)$$

$$E_{viscous} = \text{Im}[E^*] = \frac{\sigma_0}{\epsilon_0} \sin(\delta). \quad (1.14)$$

1.4.3.2 Mechanical Differences

Previous work using sonoelastography has shown significant differences in the viscoelastic properties between benign and cancer cells [22].

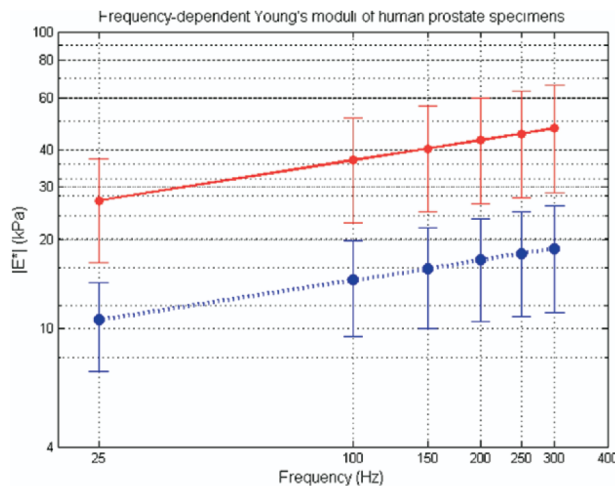


Figure 1.4: Plot of averaged magnitudes of complex Young's Moduli of normal (blue dotted curve) and cancerous (red solid curve) prostate tissue as a function of frequency. Standard deviations are also provided [22].

Figure 1.4 shows a difference in frequency-dependent resistance to mechanical stress. An incoming ultrasound wave is precisely an oscillatory mechanical stress and therefore should

interact differently with healthy and cancerous cells. Furthermore, we hypothesize that microvibrations from the room affect the propagation of ultrasound waves inside the medium differently based on the viscoelastic properties of the medium. For example, a typical table fan operates at a frequency of 2000 rpm or about 33 Hz, well within the range of frequencies shown to elicit different strain responses between healthy and cancer cells (Figure 1.4). The response of the tissue to microvibrations then interferes with the incoming ultrasound wave. This hypothesis explains the result that when RFTS methods are used on a sample on an optical table, the classification is worse than an identical experiment where the sample is placed on a regular table.

1.5 Scope and Limitations of Project

In this section, we outline the scope of the project. The ultimate goal of RFTS ultrasound research is to identify the physical mechanisms that allow Machine Learning techniques to differentiate between healthy and cancerous cells. However, in this project, we take a simplified route and investigate the ultrasound response of synthetic phantoms. The advantage of using synthetic phantoms rather than tissues is that we are able to isolate parameters to study. A inhomogeneous, dynamic system like human tissue may be too complex to apply meaningful analysis of the physics. On the other hand, a homogeneous, unchanging piece of phantom allows for careful scrutiny of the RFTS process. While the phantoms used are good experimental candidates, the reader should recognize that the conclusions we make in this report were derived from experimental results in a simplified system. We will provide, to the best of our ability, reasoning on physical grounds on how the results can extrapolated to real tissue classification; however, bear in mind that any claims about classification of real tissue are hypotheses at best and will require further investigation. Some future experiments are suggested in the recommendations chapter.

In the initial proposal for this investigation, simulation code and results using software packages such as Field-II and k-Wave were designated as part of the project deliverables. The purpose of the simulations was to emulate the effect of ambient vibrations, or noise, on the classification of synthetic phantoms. Two and a half months were allotted for simulation work while simultaneously running experiments and processing data. Due to time constraints, all of the proposed deliverables could not be met, so only the experimental component was performed. The content of this report will not contain simulation data, but will focus on the experimental methods, data analysis, and results concluded.

It is also worthwhile to note that we had no control over the physical properties of the phantoms used in the study. We used two different types of phantoms in this project: phantoms that differed in the real elastic modulus and phantoms that differed in the scatterer size. All of

the phantoms were provided by Philips and unfortunately, we had no control over the design of said phantoms. The reader should recall that in our background section on viscoelastic theory, we discussed the complexities of real tissue. Namely, it is insufficient to model real tissue as purely elastic. We must model it as a viscoelastic material with both elastic and viscous behavior. It is quite reasonable to speculate that both the elastic and viscous properties of real tissue will affect the ultrasound response. Therefore, it is likely that classification between cancerous and healthy tissues is possible because of differences in viscous behavior as well as elastic behavior. Our study only looks at phantoms that differ in their elastic properties and is limited in this sense.

EXPERIMENTAL PROCEDURE

This chapter will introduce the ultrasound equipment used and discuss the various experimental procedures performed on the Phantom samples. To investigate the effect of ambient noise on ultrasound tissue classification accuracy and explore the hypothesis presented in Section 1.3, experiments were divided into four primary sections; namely no induced noise on an undamped table, induced noise on an undamped table, no induced noise on a damped (optical) table, and induced noise on a damped table.

For each of these experimental set-ups, experiments were repeated multiple times at different ultrasound parameters. These parameters include imaging depth, focal depth, transducer power output, center frequency, and acoustic noise frequency.

2.1 Ultrasound Equipment

The ultrasound experiments designed to investigate the hypothesis of Section 1.3 were performed using an Analogic SonixTouch Ultrasound System, a L14-5/38 Linear Transducer, Philips phantoms, and an optical table. These resources were provided courtesy of our sponsor, Dr. Purang Abolmaesumi, and Philips Research North America. Their specifications will be detailed below.

2.1.1 Analogic SonixTouch Ultrasound System

2.1.1.1 System Overview

The SonixTouch Ultrasound system, as depicted in Figure 2.1 is a diagnostic ultrasound system that is able to perform a variety of imaging modes using ultrasound RF data, ranging

from the standard B (brightness) mode where display brightness is used to indicate amplitude, to the Colour/Power Doppler mode that superimposes a colour map onto the B mode to illustrate blood flow [16].



Figure 2.1: Analogic SonixTouch Ultrasonix picture obtained from http://www.ultrasonix.com/webfm_send/1121

2.1.1.2 System Components

This ultrasound system consists of a DAQ board, LCD display, touch screen on an operator console, side connectivity panel for data transfer (USB ports), and a system case capable with three transducer ports. The entire assembly is mounted on a wheelbase with four casters and has front/back handles for high mobility.

2.1.1.3 Imaging Modes

The SonixTouch is capable of performing B-mode, M-mode, Continuous Wave (CW) Doppler, Pulse Wave (PW) Doppler, and various other 3D imaging mode by acquiring ultrasound RF data. Documentation for each of these modes can be found in [1]. In the experiments described in this report, the raw ultrasound RF data was used for greater flexibility in the data analysis.

2.1.1.4 Data Post-Processing and Output

The system is equipped with native data acquisition software to perform the necessary front, mid and back-end processing to export ultrasound response data as RF files in a three dimensional matrix of data points, representing a cross section of the sample under examination over time. A third party software provided by the sponsor was used to increase the efficiency of data collection. Most of the processing was done by the native software while third party software received and

formatted the data from the native software. Among other reasons, the third party software was utilized because it had precise control over the number of frames acquired in a time period. The data files were transferred to a USB for advanced post-processing.

2.1.2 L14-5/38 Linear Transducer

2.1.2.1 Principles of Operation

The L14-5/38 transducer relies on the electro-mechanical properties of piezo-electric elements to generate sound waves and measure the reflection. During transmission, high voltage pulses traveling through the piezo-electric components produce sound waves that travel through sample tissue. During reception, miniature displacements in the elements generate small voltage waveforms. Transducers are generally expensive due to the delicate impedance matching required at the probe-skin boundary to minimize reflection.

2.1.2.2 Specifications

This transducer has a frequency range of 5-14 MHz, a focal range of 2-9 cm, and a maximum image width of 38 mm. The L14-5/38, shown in Figure 2.2 is used for imaging smaller parts of the body with high resolution but relatively shallow depth. In linear probes like this L14-5/38, the piezo-electric elements are aligned in a linear fashion, resulting in rectangular ultrasound images.



Figure 2.2: L14-5/38 Linear Transducer image obtained from <http://www.bkultrasound.com>

2.1.3 Philips Phantoms

Phantoms are tissue-simulating objects used to mimic certain properties of living tissue. In particular, the two types of phantoms used in these experiments were designed and produced by Philips Research North America. The first type of phantom is a uniform elasticity phantom with regions corresponding to tissues with different elastic moduli. The second type of phantom is a uniform scatterer phantom with different regions of scatterer sizes. The phantoms are held

	Region 1	Region 2	Region 3
Speed of Sound	1540 ± 20 m/s	1520 ± 20 m/s	1530 ± 20 m/s
Young's Modulus	35 ± 3 kPa	5 ± 1 kPa	15 ± 2 kPa
Average Scatterer Diameter	30-50 microns	30-50 microns	30-50 microns
Average Scatterer Concentration	1 g per 100 cc	1 g per 100 cc	1 g per 100 cc

Table 2.1: Uniform Elasticity Phantom Specifications

in acrylic housing with inside dimensions W20cm × L42 cm × H23 cm (see Fig. 2.3) with a Saran laminate membrane on the top surface and a 1 cm thick layer of an epoxy-based acoustic absorbing layer on the bottom of the phantom.

2.1.3.1 Uniform Elasticity Phantom

The Philips uniform elasticity phantom was made with three unique regions: one with an elastic modulus of 5 kPa, another with an elastic modulus of 15 kPa, and the third with an elastic modulus of 35 kPa. These regions were designed to be homogeneous, **with scatterer sizes constant across all three sections**. A graphic illustrating the elasticity phantom can be seen in Figure 2.3. Speed of sounds, average scatterer diameter and average scatterer concentration can be found in 2.1.3.1.

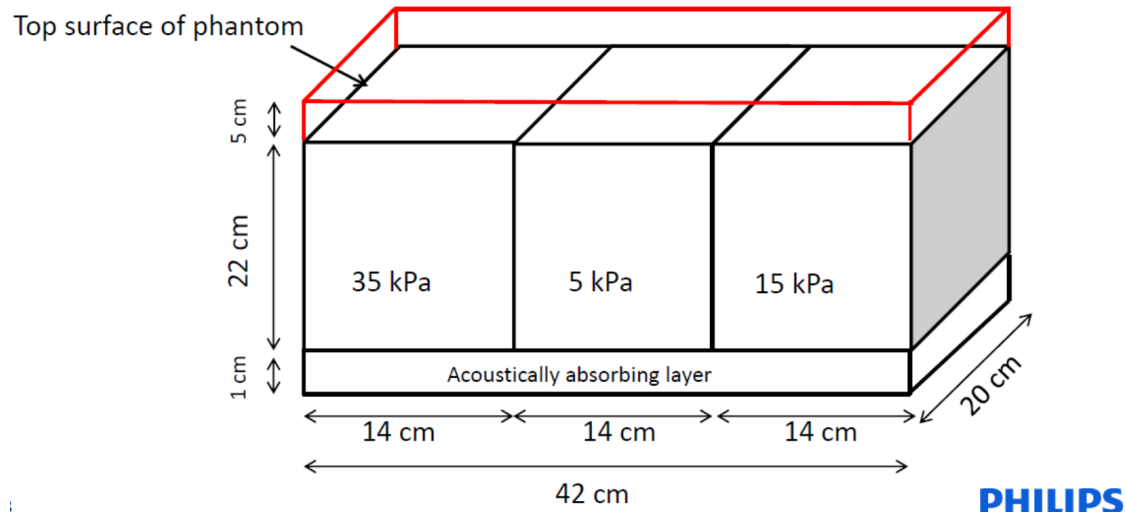


Figure 2.3: Diagram showing the elastic moduli and dimensions of the uniform elasticity phantoms. Figure courtesy of Philips Research North America.

2.1.3.2 Uniform Scatterer Phantom

The Philips uniform scatterer phantom was constructed using two unique regions: one with scatterer sizes of 7 – 10 μm and the other with scatterer sizes of 30 – 50 μm . Again, this phantom

	Region 1	Region 2
Speed of Sound	1540 ± 10 m/s	1540 ± 10 m/s
Young's Modulus	25 ± 5 kPa	25 ± 5 kPa
Average Scatterer Diameter	7-10 microns	30-50 microns
Average Scatterer Concentration	1 g per 100 cc	1 g per 100 cc

Table 2.2: Uniform Scatterer Phantom Specifications

has homogeneous regions, except in this case, the elastic modulus across the two sections is a constant. A visualization of the scatterer phantom can be seen in Figure 2.4. Speed of sounds, elastic modulus and average scatterer concentration can be found in 2.1.3.2.

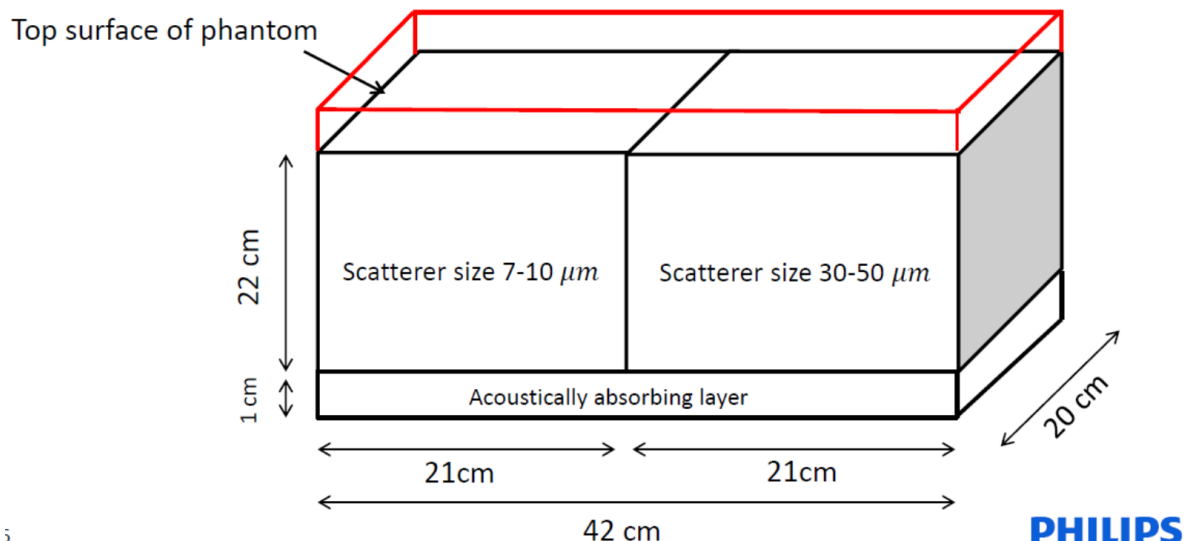


Figure 2.4: Diagram showing the scatterer size and dimensions of the uniform scatterer phantoms. Figure courtesy of Philips Research North America.

2.1.3.3 Optical Table

The optical table used in the experiments was a Newport Electronic Vibration Isolation System. The optical table has a 24" \times 36" surface and has 8 active damping elements. Unfortunately, we do not have access to the specifications for this model of the Newport optical table. An image of the table can be seen in Figure 2.5.

2.2 Experiments without Induced Noise

The first type of experiments completed were without induced noise. This condition explores classification accuracy in the absence of any significant ambient disturbance. This experiment



Figure 2.5: Newport Electronic Vibration Isolation System (Optical Table) image obtained from <http://www.lightglassoptics.com>

setup consisted of the ultrasound machine, transducer, and sample phantom. A small amount of acoustic gel was also applied at the transducer-phantom interface to couple the transducer to the phantom and maximize the acoustic propagation. A block diagram of the apparatus can be seen in Figure 2.6.

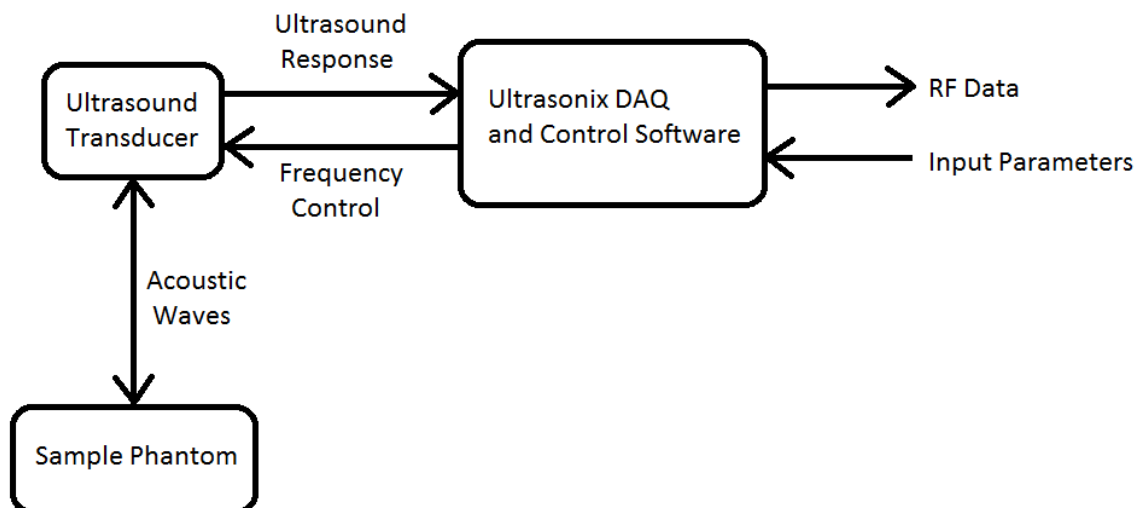


Figure 2.6: This figure illustrates the work flow of our experiments without induced noise. The block diagram consists of the ultrasound machine, transducer, and phantom.

Small microvibrations from the room are still present, so a further subcategory involved

performing experiments on an undamped table, and then on a damped optical table. On an undamped table, the transducer picks up vibrations both from the response of the tissue to the input acoustic waves as well as a small amount of ambient noise from the environment. An image of this low noise setup on an undamped table can be seen in Figure 2.7. In the other case on a damped optical table, shown in Figure 2.8, the table theoretically eliminates most of the ambient noise, acoustically isolating the response of the tissue in the transducer readings. The comparison between these two experimental cases yields information on the effect of low ambient noise levels on classification accuracy.



Figure 2.7: This figure is an image of the undamped experiment without induced noise setup. The Ultrasonix machine in the foreground is linked to the transducer positioned perpendicularly on the phantom sample. This phantom shown here is the uniform elasticity phantom with three unique regions.



Figure 2.8: This figure is an image of the damped experiment without induced noise setup. Similar to the undamped setup, the transducer is placed **perpendicular to the phantom interface**. The phantom in this image is the uniform scatterer phantom with two unique regions.

2.3 Experiments with Induced Noise

The second type of experiments were performed with induced noise, investigating classification accuracy in the presence of a significant, steady-state ambient disturbance. Similar to the setup without induced noise, the apparatus used consisted of the ultrasound machine, transducer, and sample phantom except this time, a Labtec Spin 95 speaker was used to generate steady state noise. The intensity of the induced noise was difficult to specify through the convolution of both the computer and the speaker's volume control, so the amplitude of noise across all experiments of this type was held constant. A small amount of acoustic gel was also applied at the transducer-phantom interface to maximize the acoustic propagation. A block diagram of the apparatus can be seen in Figure 2.9.

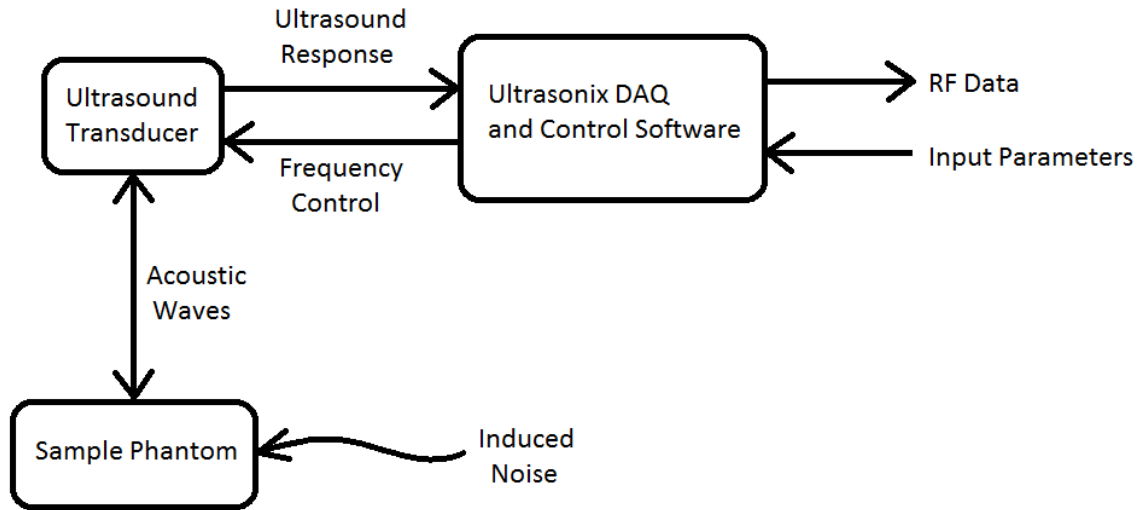


Figure 2.9: This figure illustrates the work flow of our experiments with induced noise. The block diagram consists of the ultrasound machine, transducer, phantom, and induced noise to the phantom.

Again, the experiments were conducted on an undamped table, and then on a damped optical table. On an undamped table, the transducer picked up vibrations both from the response of the tissue to the input acoustic waves, the input steady state noise from the speaker, and a small amount of ambient noise from the environment. An image of this high noise setup on an undamped table can be seen in Figure 2.10. In the other case on an optical table, shown in Figure 2.11, the table acoustically isolates the response of the tissue and the input steady state noise in the transducer readings. The comparison between these two experimental cases with the previous experiment type yields information on the effect of high ambient noise levels on classification accuracy.

2.4 Experiment Set I

The first set of experiments were performed at a constant input frequency of 6.6 MHz, 0 power setting on the Ultrasonix machine (minimum power), and focal depth of 3 cm on a regular table and an optical table. For experiments without noise, the only parameter changed between experimental setups was the imaging depth, which varied between 4 – 6cm. A table of these experiments can be seen in table 2.4.

With induced noise, experiments with steady state noise frequencies of 80 Hz and 100 Hz were conducted, as seen in Table 2.4. At each setting, 5 data sets were collected. Due to time constraints, the induced noise experiments were only run at an imaging depth of 4 cm.

Experiments without Induced Noise (5 trials per case)		<i>Image Depth (cm)</i>			<i>Table Type</i>
<i>Elasticity Phantom</i>	5 kPa	4	5	6	Undamped Damped
	15 kPa	4	5	6	Undamped Damped
					Undamped Damped
	35 kPa	4	5	6	Undamped Damped
					Undamped Damped
<i>Scatterer Phantom</i>	7-10 μm	4	5	6	Undamped Damped
					Undamped Damped
	30-50 μm	4	5	6	Undamped Damped
					Undamped Damped

Table 2.3: This table lists the experiments run without induced noise where the imaging depth was varied from 4 to 6 cm while input frequency was a constant 6.6 MHz and power setting unchanged at 0 on the Ultrasonix Machine. All experiments were run on and off an optical table.

Experiments with Induced Noise (5 trials per setup)		<i>Image Depth (cm)</i>		<i>Noise Frequency (Hz)</i>	<i>Table Type</i>	
<i>Elasticity Phantom</i>	5 kPa	4		80	100 Undamped Damped	
	15 kPa	4	80	100	Undamped Damped	
					Undamped Damped	
	35 kPa	4	80	100	Undamped Damped	
					Undamped Damped	
<i>Scatterer Phantom</i>	7-10 μm	4		80	100 Undamped Damped	
		4		80	100 Undamped Damped	

Table 2.4: This table summarizes the experiments performed with induced noise. Again, the input parameters were held constant to 6.6 MHz and 0 power setting. Induced noise was varied between 80 Hz and 100 Hz, and imaging depth was held at 4 cm. All experiments were conducted on and off an optical table.



Figure 2.10: This figure is an image of the undamped experiment with induced noise setup. The transducer is positioned perpendicularly on the phantom sample, beside a speaker emanating a low frequency tone to emulate steady-state noise. This phantom shown here is the uniform elasticity phantom with three unique regions.



Figure 2.11: This figure is an image of the damped experiment with induced noise setup. The Ultrasonix machine on the left is sending and receiving data from the transducer placed perpendicular to the phantom interface. Again, the speaker placed on top of the phantom is emitting a low frequency tone. The phantom in this image is the uniform scatterer phantom with two unique regions.

2.5 Experiment Set II

The second set of experiments were designed to investigate the different transducer input frequencies and power settings on and off the optical table. Input frequency was varied between 6.6 MHz and 10.0 MHz and the power setting on the Ultrasonix Machine was changed between 0 and -3. This time, for experiments without noise, the only parameter changed between experimental setups the focal depth, which was either 3 or 5 cm with imaging depth held at 6 cm. With induced noise, experiments with steady state noise frequencies of 80 Hz were conducted. A table of these experiments can be seen in table 2.5 Experiments with induced noise frequency of 100 Hz were not performed and only 3 data sets per setup were collected due to time constraints.

Experiment Set II (3 trials per setup)		<i>Image Depth</i> (cm)		<i>Focal Depth</i> (cm)		<i>Noise Frequency</i> (Hz)		<i>Table Type</i>
<i>Elasticity Phantom</i>	5 kPa	6	3	5	No Noise	80	Undamped	
							Damped	
	15 kPa	6	3	5	No Noise	80	Undamped	
							Damped	
	35 kPa	6	3	5	No Noise	80	Undamped	
							Damped	
<i>Scatterer Phantom</i>	7-10 μ m	6	3	5	No Noise	80	Undamped	
							Damped	
	30-50 μ m	6	3	5	No Noise	80	Undamped	
							Damped	

Table 2.5: This table summarizes the experiments conducted with varying input frequency and power. For each permutation of 6.6 or 10 MHz and 0 or -3 power, the experiments listed in this table were performed. Image depth was held constant at 6 cm, focal depth was varied between 3 and 5 cm, and induced noise was either turned off or set at 80 Hz. All experiments were run both on and off an optical table.

ANALYSIS, RESULTS, AND DISCUSSION

This section will detail how the ultrasound RF data files acquired from the experiments described in Chapter 2 were analyzed to determine classification accuracy between various Phantom samples of different elasticities and scatterer ("cell") sizes. The main stages of data analysis, visualized in Figure 3.1 were feature extraction from the RF files, data cleansing to filter out anomalous feature data, and tissue classification using these feature files and a support vector machine (SVM).



Figure 3.1: This figure illustrates the data analysis flow of raw data through feature analysis, data cleansing, classification with a support vector machine, resulting in classification accuracy of a particular data set.

3.1 Feature Extraction

Before running any classification algorithm, we extracted useful data from the raw data files outputted by the Ultrasound machine. This *useful* data is referred to as the features of a particular experimental data set. The features have been defined by previous work done by the project sponsor [10, 11, 18] and will be detailed in the following subsections. Note that we adhere to the same feature numbering convention as our project sponsor, and that all of the MATLAB code to extract features was also provided by the sponsor.

3.1.1 Regions of Interest (ROIs)

As part of our feature extraction process, we defined Regions of Interest (ROIs), in order to increase the efficiency of the analysis. This optimization is necessary since the raw data is a 3-Dimensional Matrix data-type (MATLAB) with the size of the matrix as $N \times M \times T$: N = number of axial pixels ≈ 1500 , M = number of lateral pixels = 256, T = number of frames ≈ 150 . We chose our ROI's as ± 0.5 mm from the focal depth setting of the ultrasound machine and sectioned off this focal region into unit ROI squares of $1 \times 1 \text{ mm}^2$ in area.

Based on the axial resolution of the RF data of 52 data points (pixels) per mm and 256 scan lines (also = number of pixels) from the transducer of width 38 mm (see Sec. 2.1.2), each ROI was determined to be a 52×7 matrix of data points. The maximum number of ROI's that could fit across the focal region of 10×38 mm, or a 520×256 matrix, was 360, which left an insignificantly small part of the data and features were then extracted for all 360 of these regions of interest. All in all, per ROI we have a 52×7 , with 360 total ROIs, and reduces the volume of data analyzed by a factor of ≈ 3 .

3.1.2 Fast Fourier Transform

In many time-series data analyses it is interesting to consider the frequency components of the signal – transform the data into the Fourier domain. Considering frequency components oftentimes provide insights to the data in question otherwise unseen in the time-domain.

For most of our data analysis we worked with MATLAB, and in-turn used MATLAB's `fft()` function, which implements the Fast-Fourier Transform algorithm (FFT). The FFT computes the DFT (Discrete Fourier Transform), and produces exactly the same result as evaluating the DFT directly. The most important property of the FFT Algorithm is that the FFT has a much faster run-time: $\mathcal{O}(T \log T)$ as opposed to the DFT's $\mathcal{O}(T^2)$, where T denotes the number of time-domain sample points.

In MATLAB, it is defined as:

$$Y(k) = \sum_{j=1}^T X(j) \exp\left(\frac{-2\pi i(j-1)(k-1)}{T}\right) = \mathcal{F}[X](k). \quad (3.1)$$

Where $X(j)$ is your time-series input data, and $Y(k)$ is your Fourier-transformed output. Oftentimes, $Y(k)$ is referred to as the *spectrum* of a time-domain signal vector $X(j)$.

3.1.3 Features 1 – 4: Frequency Domain Quadrants

Before defining the features themselves, first we will describe how the spectrum is constructed, as there is a little bit more than just applying the FFT to a given pixel data point.

Let r be the current ROI number, with $r \in \{1, 2, \dots, 360\}$. Let the ROI data matrix, R^r , be of size $N \times M \times T$, with $N = 52$, $M = 7$, and $T = \text{Number of Frames} - (\text{Number of Frames mod } 8)$, hence T has the following property: $T = 0 \bmod 8$. T is defined such that later on it is ensured that the spectrum can be evenly divided into 4 parts. Everything thus far is formalized from the discussion in Section 3.1.1.

Let $X_{nm}^{(r)}$ be a vector of the time-series data at the local pixel location (n, m) in R^r of length T . The top-left of the R^r is $(1, 1)$, top-right is $(1, M)$. The third dimension is left out because all points are considered in the temporal domain (that's why $X_{nm}^{(r)}$ has length T).

Now, we continue to our first step of processing. We subtract the mean of $X_{nm}^{(r)}$, $\mu_{nm}^{(r)}$, from $X_{nm}^{(r)}$ and apply a Hamming window in order to give more weight to temporal points nearer to the middle of the vector – this is to say, we weigh the data when the transducer starts up and turns off, less. In equation form,

$$\bar{X}_{nm}^{(r)} = \text{Hamming}[X_{nm}^{(r)} - \mu_{nm}^{(r)}]. \quad (3.2)$$

The next steps are to apply the FFT, sum up the results for that specific ROI, and then take an average, followed by a normalization. The average is taken because we can then assign that spectrum to a certain ROI and to smooth out any noisy data that might appear in a pixel by pixel analysis. After averaging, we normalize the data so that we can compare the results between ROIs more meaningfully. In equation form,

$$Y_{nm}^{(r)} = \mathcal{F}[\bar{X}_{nm}^{(r)}], \quad (3.3)$$

where $Y_{nm}^{(r)}$ is length $T/2$ (this is because the FFT is periodic, so we do not consider more than one period of it). Note is that $Y_{nm}^{(r)} \in \mathbb{C}$, so we consider the 2-norm squared of it,

$$S^{(r)} = \sum_{n,m} \frac{\|Y_{nm}^{(r)}\|_2^2}{\text{number of pixels in ROI } r}, \text{ and normalizing,} \quad (3.4)$$

$$\bar{S}^{(r)} = \frac{S^{(r)}}{\max S^{(r)}}. \quad (3.5)$$

The final step before defining the features is to combine all Now we are ready to define the features per ROI r : $\mathbf{F}_1^{(r)}$, $\mathbf{F}_2^{(r)}$, $\mathbf{F}_3^{(r)}$, and $\mathbf{F}_4^{(r)}$. They are defined as the sum of the spectrum points in each respective quadrant of the spectrum. In other words, we divide the spectrum into 4 regions, and sum the points there. **The idea of the summing it is proportional to the integral of the spectrum which is related to the average power of the signal.** So finally, we get:

$$\mathbf{F}_i^{(r)} = \sum_{k=1+(i-1)\frac{T}{8}}^{i\frac{T}{8}} \overline{S(k)}^{(r)} \text{ for } i = 1, 2, 3, 4. \quad (3.6)$$

3.1.4 Features 5 & 6: Linear Fit to Fourier

The next two features again deal with the spectrum of the time-series vector $X_{nm}^{(r)}$, defined in the above section. Features \mathbf{F}_5 and \mathbf{F}_6 are the slope and y -intercept of the linear fit to $\overline{S}^{(r)}$, defined in Equation 3.5. Therefore in equation form,

$$\overline{S}_{\text{linear}}^{(r)}(k) = \mathbf{F}_6 k + \mathbf{F}_5. \quad (3.7)$$

It is important for the reader to note that features \mathbf{F}_5 , \mathbf{F}_6 are highly dependent on the first four, \mathbf{F}_1 , \mathbf{F}_2 , \mathbf{F}_3 , and \mathbf{F}_4 . We will see this dependency again during the analysis of the results (Sec. 3.4.6).

3.1.5 Feature 7: Fractal Dimension

The next feature is less physical than the first six, it deals with the physical shape of the time-series curve. The definition of the fractal dimension is:

$$\text{Fractal Dimension} = \frac{\log(\text{number of self-similar segments})}{\log(\text{magnification factor})}. \quad (3.8)$$

Equation 3.8 is difficult to digest at first, but it becomes clearer with an example. The notion of the fractal dimension generalizes the idea of dimensionality to include fractal patterns, such as the Sierpinski triangle. As we know that a line-segment as $n = 1$, a square has $n = 2$, a cube has $n = 3$, and so on. To see how equation 3.8 comes into this, consider the case of a square. Suppose you have a square of side length N . We can decompose the square into N^2 different sub-squares by making a grid of spacing $1/N$ on each side. **However, if we scale up the entire picture by a factor of N , we can see that one of the sub-squares is identically equal to the square we started with.** Applying equation 3.8 to this case we get $\frac{\log(N^2)}{\log(N)} = 2$.

In terms of the data analysis, the feature is exactly the ROI average of the F.D. of $X_{nm}^{(r)}$ (defined in Sec. 3.1.3). In equation form,

$$\mathbf{F}_7 = \sum_{n,m} \frac{\text{F.D.}[X_{nm}^{(r)}]}{\text{number of pixels in ROI } r}, \quad (3.9)$$

where $\text{F.D.}[\cdot]$ denotes a function that calculates the fractal dimension of a vector. In our analysis, we used a MATLAB function which implements an algorithm that calculates the F.D. for a given vector. This function was given to us by the sponsor to use.

3.1.6 Feature 8: Spectrum Dot Product

Feature number 8 is exactly the spectrum dot product with the frequency axis, divided by the sum of the spectrum. So in equation form,

$$\mathbf{F}_8 = \frac{\omega \cdot \bar{S}^{(r)}}{\sum_k \bar{S}^{(r)}(k)}, \quad (3.10)$$

where ω is a vector of the frequency axis (length $T/2$), and $\bar{S}^{(r)}$ defined in Section 3.1.3. Since this feature uses the spectrum, it is expected that it is correlated highly with the first six features: $\mathbf{F}_1, \mathbf{F}_2, \mathbf{F}_3, \mathbf{F}_4, \mathbf{F}_5, \mathbf{F}_6$ - which is what we observe in Sec. 3.4.6.

3.1.7 Feature 9: Daubenchies Wavelets

The final feature is decomposing the signal $X_{nm}^{(r)}$ into a certain set of basis functions, called Daubenchies Wavelets, and then approximating the coefficients in which the linear combination of Daubenchies Wavelets are able to reconstruct $X_{nm}^{(r)}$ – in fact we only take the first of these coefficients. Finally the coefficient is averaged and the final feature is constructed. This process is a Discrete Wavelet Transform and is a popular technique in texture classification problems (medical imaging, image databases, etc.) and is used often [2]. So in equation form,

$$\mathbf{F}_9 = \sum_{n,m} \frac{\text{W.T.}[X_{nm}^{(r)}]}{\text{number of pixels in ROI } r} \quad (3.11)$$

where W.T.[] computes the Daubenchies Wavelet Transform and extracts the first Daubenchies Wavelet Coefficient (code provided by sponsor).

3.2 Data Cleansing

Before we performed classification, we plotted the displacement versus time. One of these figures is shown in Fig. 3.2. As seen from the bottom of Figure 3.2, there are anomalous structures in the displacement of the regular 7-10um5cm sample. We believe this structure comes from a problem with the data acquisition process, but the exact origin is uncertain. We suspect it might be sudden movements or shaking of the table during data acquisition that caused the jumps in displacement. Fortunately, these structures are rare and only occur about once every 30 trials. Nevertheless, we created a data cleansing algorithm to identify the files with anomalous structure and remove them from the set for classification.

We defined a data set to have anomalous structure if its ultrasound signal fluctuates unreasonable high. To be more specific, we defined an indicator function to measure the quality of the data:

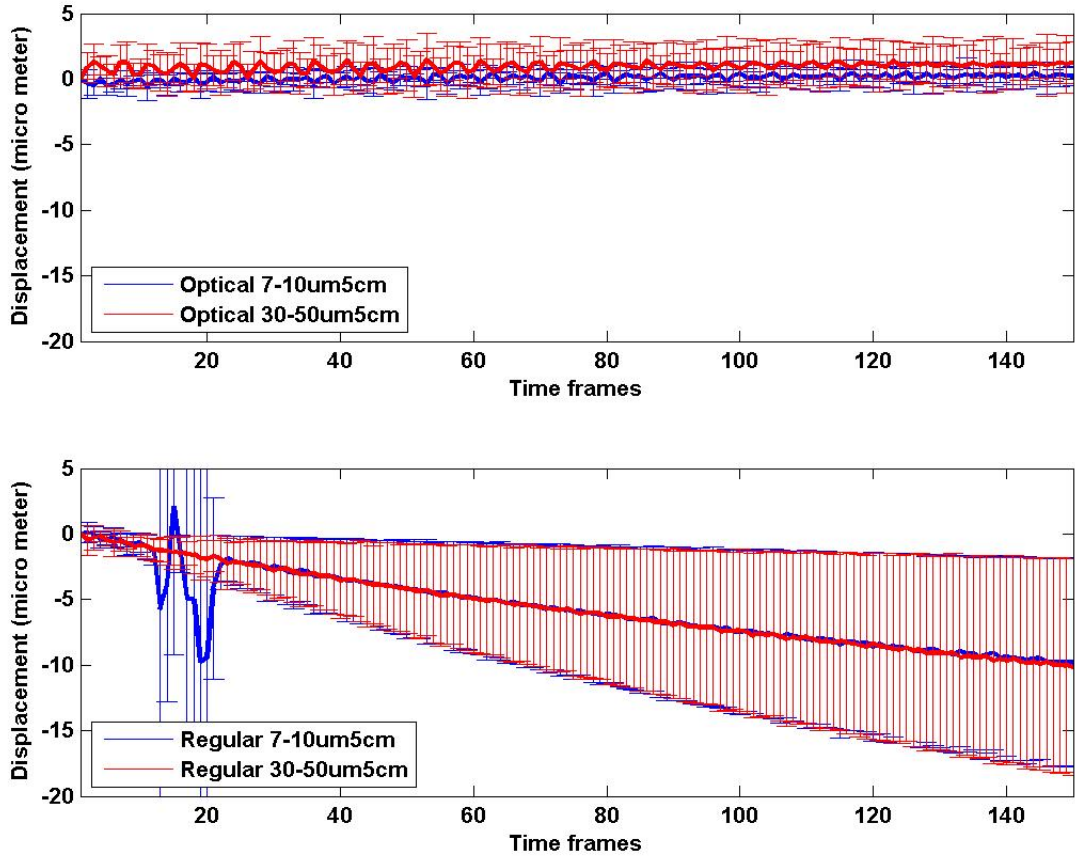


Figure 3.2: This figure shows the displacement for different experimental setups. There is anomalous structure for the 7-10um experiment done on the regular table as seen by the fluctuation of the blue line in the bottom graph.

$$\text{Indicator Signal}(t) = 10^{f(\text{Raw}(t))} \quad (3.12)$$

Here t is the frame number, $\text{Raw}(t)$ is the raw ultrasound signal and $f(x)$ is a linear transformation. An example of this function is plotted for ten trials of one of our experimental setups (see Fig. 3.3). As we can see from Figure 3.3, one of the trials has a much higher indicator signal than the other nine trials, indicating that it should be removed from the classification set. The criteria for discarding a data set was: if its maximum indicator signal was one order of magnitude greater than the maximum indicator signal of the other nine trials, then remove it. **While this is not, in general, a rigorous method for rejecting data sets, it was sufficient for our case for two reasons.** First, very few files had the anomalous structure (≈ 1 in 30) and hence rejecting files incorrectly would not significantly hurt the classification. Second, the structure was usually quite obvious because there was often much greater than one order of magnitude difference in indicator signal

and the structure is spread over tens of time frames.

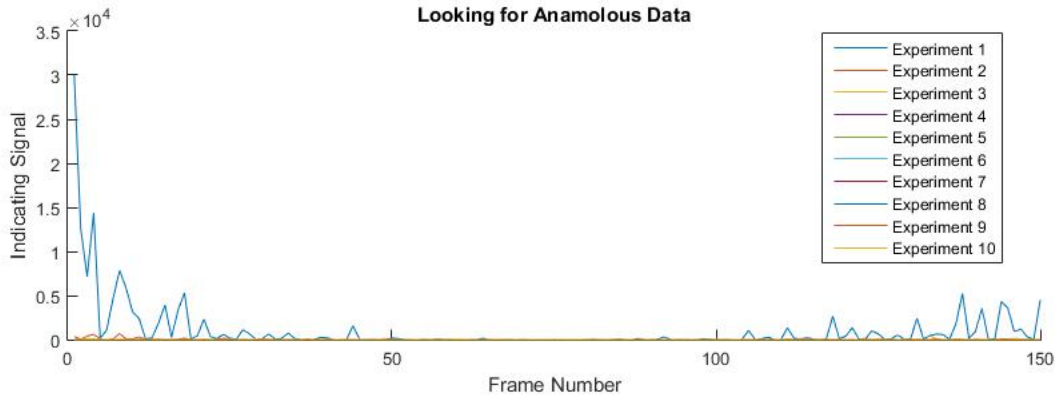


Figure 3.3: This figure shows indicator signal as defined above plotted against the time frame. A high indicator signal suggests a problem with the data acquisition process. Here experiment 8 was rejected and taken out of the set of data used in classification.

3.3 Tissue Classification with a SVM

A note to the reader: This section can be skipped without losing continuity in the report. This section is included for the curious reader who is interested in how the Machine Learning works.

3.3.1 SVM Code Library

Classification was performed using the LIBSVM developed by Chih-Chung Chang and Chih-Jen Lin (<https://www.csie.ntu.edu.tw/~cjlin/libsvm/>). The SVM algorithm is a supervised learning algorithm where data points are passed in with labels. In other words, we inputted vectors containing ultrasound features and for each vector, labeled it as phantom type I or phantom type II. The aim of the SVM algorithm is to learn the set of weights w of a predictive model. It learns these weights by minimizing a loss function over w in parameter (weight) space. The loss function penalizes the model for predicting the wrong class and hence over time the model "learns" to use the best weights for prediction. In parameter w space, the loss function can be written as,

$$L(w) = \sum_{i=1}^N \max \{0, 1 - y^i w^T x^i\} + \frac{\lambda}{2} \|w\|^2 \quad (3.13)$$

The first term on the right hand side is usually called the hinge-loss. Here x^i is the i^{th} training data point (which is a vector of features) and y^i is the label for that training point (a scalar). w^T is the transpose of the vector of weights we are trying to learn and λ is a regularization that prevents the model from over-fitting. Finally, $\|\cdot\|$ is the 2-norm. The loss function stated above limits the model to linear functions in feature-space. That is, we are limited to the set of

models that are hyper-planes in feature-space. In order to increase the complexity of the model, a Gaussian kernel is used to transform the data points x^i before classification. A common algorithm used to solve supervised learning problems is gradient descent which iteratively improves the model weights w ,

$$w^{t+1} = w^t - \nabla L(w) \quad (3.14)$$

Model weights w are being updated at each time step according to the update above. However, LIBSVM runs an optimized version of the algorithm. LIBSVM converts the loss function in parameter space, also known as the primal problem, into a function to be optimized in dual-space. This function existing in dual-space is called the Fenchel dual of the primal problem and for the SVM formulation is,

$$D(z) = e^T z - \frac{1}{2\lambda} z^T \text{Diag}(y) X X^T \text{Diag}(y) z \quad s.t. \quad 0 \leq z_i \leq 1 \quad \forall i \quad (3.15)$$

Here z is the dual-space parameter we are optimizing, e^T is a vector of ones, $\text{Diag}(y)$ is a diagonal matrix constructed from all N class labels, X is the data matrix containing all N data points. Gradient ascent is performed on this Fenchel dual problem to find the optimal weights of the SVM predictive model.

There are several reasons why converting the primal problem to the dual problem improves the SVM algorithm. First, the loss function in parameter space is non-smooth. But because it is strongly convex, the Fenchel dual is guaranteed to be a smooth function. Gradient methods are able to optimize smooth functions quicker than non-smooth ones. Second, converting the primal problem into the dual problem may lower the dimension of the model weights to be solved. That is, the dimension of the z vector is less than that of the w vector. This also speeds up the SVM algorithm. Finally, the solution of the Fenchel problem is sparse, meaning that many of the weights in the z vector are actually 0 and hence we get a simpler model which still accurately describes our data. Please refer to LIBSVM documentation for more implementation details [3].

3.4 Results

3.4.1 Classification Results: Data Set I

In the first data set, we performed leave-one-out cross-validation with 5 feature files per phantom type or 10 files in total. For example, consider a classification between the 5kPa and 35kPa phantoms. On the first iteration, the SVM algorithm will only **train on 4 of the 5 feature files of 5kPa and 4 of the 5 files of 35kPa**. There are $360 \times 8 = 2880$ training data points, 1440 for each class. The file that was left out was used as a test data set to measure the quality of the model. The results of the classification are shown in Figure 3.4.

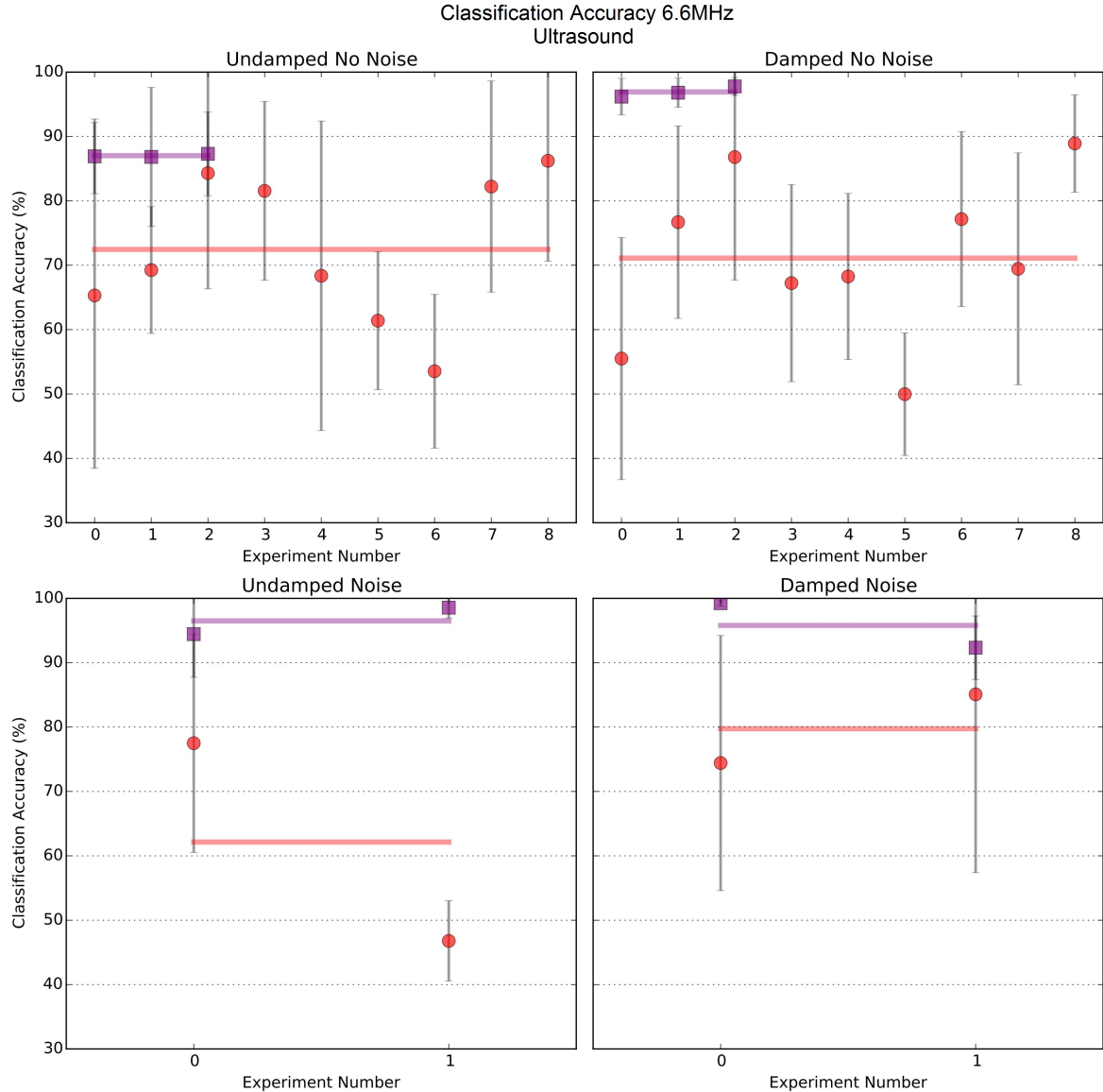


Figure 3.4: This figure shows average (over 5 trials) classification accuracy. Each quadrant shows a different experimental setup. The x -axis enumerates the different experiments. Tables 3.1 and 3.2 show the exact experiments the numbers represent. **Purple squares represent experiments conducted on scatterer phantoms** while red circles represent experiments on elasticity phantoms. The purple and red lines represent the mean (over all experiments in plot) accuracy. Uncertainty bars are shown and indicate the amount of variance in classification accuracy between trials for the same experiment.

For Elasticity Phantoms the average classification accuracy was about 70%. There were large variances between trials as seen in the uncertainty bars of Figure 3.4. For the no noise case, mean classification accuracy is approximately the same with (71%) and without the optical table (72%).

Experiment Number	Elasticity Experiments No Noise	Elasticity Experiments Noise
	<i>Experiment Settings</i>	<i>Experiment Settings</i>
0	No-noise_15kpa4cm_35kpa4cm	Noise_15kpa4cm100hz_35kpa4cm100hz
1	No-noise_15kpa4cm_5kpa4cm	Noise_15kpa4cm80hz_35kpa4cm80hz
2	No-noise_15kpa5cm_35kpa5cm	
3	No-noise_15kpa5cm_5kpa5cm	
4	No-noise_15kpa6cm_35kpa6cm	
5	No-noise_15kpa6cm_5kpa6cm	
6	No-noise_35kpa4cm_5kpa4cm	
7	No-noise_35kpa5cm_5kpa5cm	
8	No-noise_35kpa6cm_5kpa6cm	

Table 3.1: Legend for elasticity experiments in Figure 3.4. The numbering is the same for damped and undamped experiments.

Experiment Number	Scatterer Experiments No Noise	Scatterer Experiments Noise
	<i>Experiment Settings</i>	<i>Experiment Settings</i>
0	No-noise_30-50um4cm_7-10um4cm	Noise_30-50um4cm100hz_7-10um4cm100hz
1	No-noise_30-50um5cm_7-10um5cm	Noise_30-50um4cm80hz_7-10um4cm80hz
2	No-noise_30-50um6cm_7-10um6cm	

Table 3.2: Legend for scatterer experiments in Figure 3.4. The numbering is the same for damped and undamped experiments.

For the induced noise case, there is a 18% difference in classification between the damped (80%) and undamped (62%) case. However, the mean classification accuracy of the damped experiments lies within the uncertainty bars of the undamped experiments and vice-versa. Therefore, we cannot conclude a significant change in classification accuracy for this case. Comparing the top two against the bottom two graphs of Figure 3.4, we see no conclusive effect of induced noise on accuracy. In the damped case inducing noise improves classification by 19%. On the other hand in the undamped case inducing noise worsens classification by 10%. In both cases, the mean classification accuracy of one graph lied within most of the uncertainty bars in the other experiment. Hence, we can say that inducing noise has minimal effect on classification accuracy for the elasticity phantoms. The large uncertainty bars indicate that there is a large spread in the classification accuracy between trials. This could imply that the machine learning algorithm is separating classes based on artifacts rather than differences in signal. We continue the discussion of the uncertainties in Section 3.4.3.

For Scatterer Phantoms the mean classification accuracy was between 87%-97% with small variance between trials. Looking at Figure 3.4 noise has little effect on classification on an optical table, but in absence of noise, optical table improves classification. Inducing noise significantly improves classification accuracy on a regular table. Understanding the above results needs the

	Elasticity Experiments No Noise	Elasticity Experiments Noise
Experiment Number	Experiment Settings	Experiment Settings
0	No-noise 15kpaF3cm_35kpaF3cm	Noise 80Hz15kpaF3cm_35kpaF3cm
1	No-noise 15kpaF5cm_35kpaF5cm	Noise 80Hz15kpaF5cm_35kpaF5cm

Table 3.3: Legend for elasticity experiments in Figures 3.6 and 3.5. The numbering is the same for damped and undamped experiments.

	Scatterer Experiments No Noise	Scatterer Experiments Noise
Experiment Number	Experiment Settings	Experiment Settings
0	No-noise 30-50umF3cm_7-10umF3cm	Noise 30-50umF3cm_7-10umF3cm
1	No-noise 30-50umF5cm_7-10umF5cm	Noise 30-50umF5cm_7-10umF5cm

Table 3.4: Legend for scatterer experiments in Figures 3.6 and 3.5. The numbering is the same for damped and undamped experiments.

theory described in Section 3.4.8. There are a few things to be explained, first we explain why the Scatterer Phantoms are classified better than the Elasticity Phantoms. We have many features that deal with the spectrum, namely $\mathbf{F}_1, \mathbf{F}_2, \mathbf{F}_3, \mathbf{F}_4, \mathbf{F}_5, \mathbf{F}_6$, and \mathbf{F}_9 (defined in Section 3.1.3). The **power of the echo, or power spectrum, is directly related to scatterer size**, as seen in Equation 3.17. Since we are changing the size of the scatterers in these experiments, the separation will be much more distinct than in the case of Elasticity Phantoms – hence leading to the $\approx 20\%$ increase in classification accuracy. The next result that is intriguing is that the addition of noise on the undamped table increases the classification accuracy. This can also be explained with the theory in Section 3.4.8. The addition of noise simply means more amplitude for certain frequency components in the power spectrum. So the addition of noise increases the energy of echos the probe is receiving – giving a more pronounced separation, hence increasing the classification accuracy. The pronounced separation is also visible in Fig. 3.16 (undamped table, 80 Hz).

3.4.2 Classification Results: Data Set II

We collected a second set of data in order to investigate the effect of ultrasound frequency and power on classification accuracy. In the second data set, we performed leave-one-out cross-validation with 3 feature files per phantom type or 6 files in total. Due to time constraints we were unable to collect more than three trials per experiment. This was due to a bottleneck in the amount of time it took the software to process the data. There are $360 \times 4 = 1440$ training data points, 720 for each class. The file that was left out was used as a test data set to measure the quality of the model. The results of the classification for 10MHz ultrasound output and 0 power setting is shown in Figure 3.5. The results of classification for 6.6MHz output and 3 power is shown in Figure 3.6.

Due to time constraints we were unable to collect more than three trials per experiment.

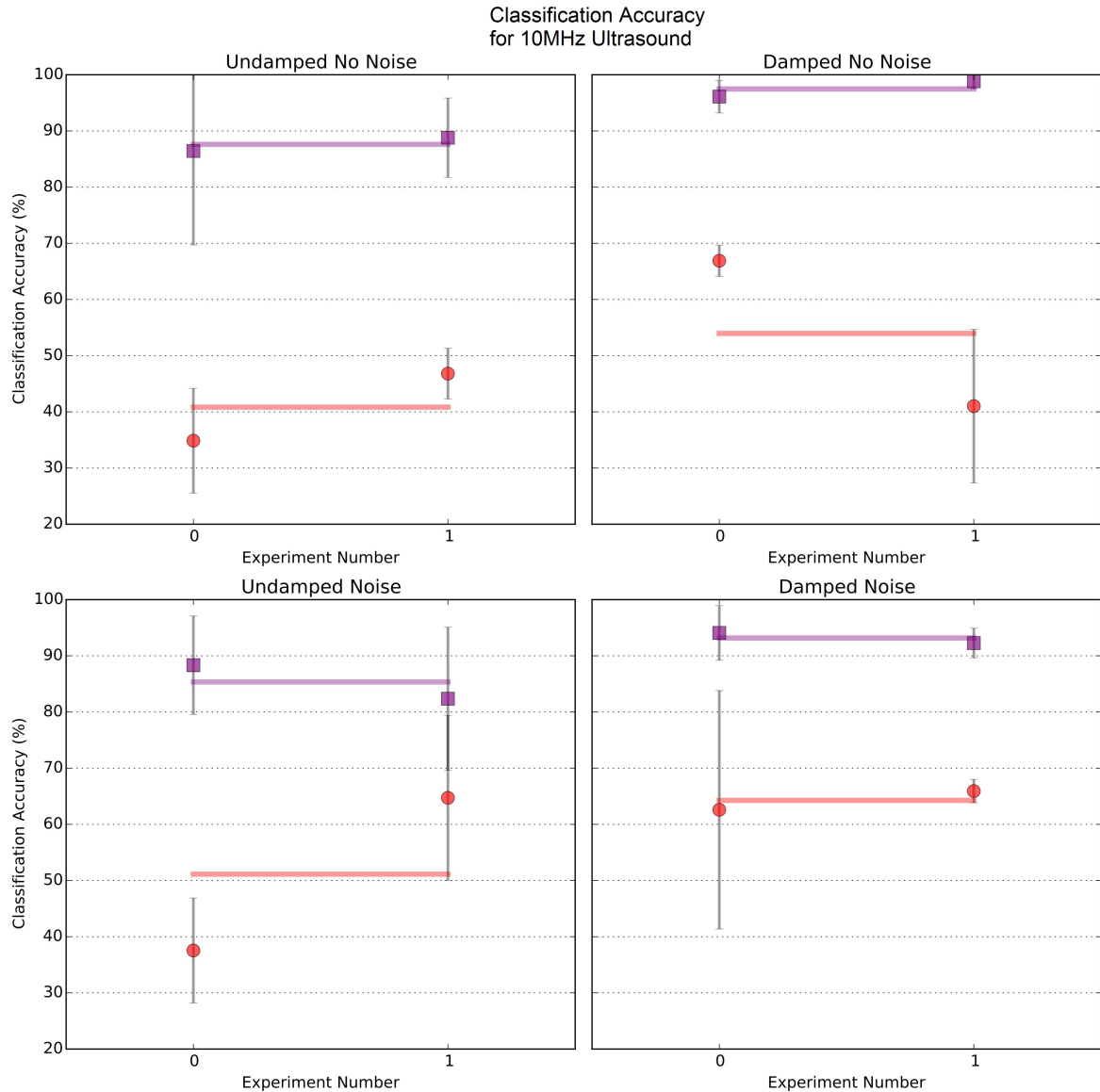


Figure 3.5: This figure shows average (over 3 trials) classification accuracy for the 10MHz, 0 power setting. Each quadrant shows a different experimental setup. The *x*-axis enumerates the different experiments. Tables 3.3 and 3.4 show the exact experiments the numbers represent.

Despite the fewer number of trials taken (and hence fewer training points for the SVM), scatterer phantoms are able to be classified with almost the same accuracy, as in data set I. This suggests real physical differences in the ultrasound response between phantoms with different scatterer sizes, as discussed in Section 3.4.1 (model discussed in Section 3.4.8). On the other hand, elasticity phantoms cannot be classified with leave-one-out cross-validation with 3 feature files per phantom type. 50% is the classification accuracy means that it's the same as randomly guessing the classes. Only 2 out of the 8 elasticity experiments have classification accuracy greater than

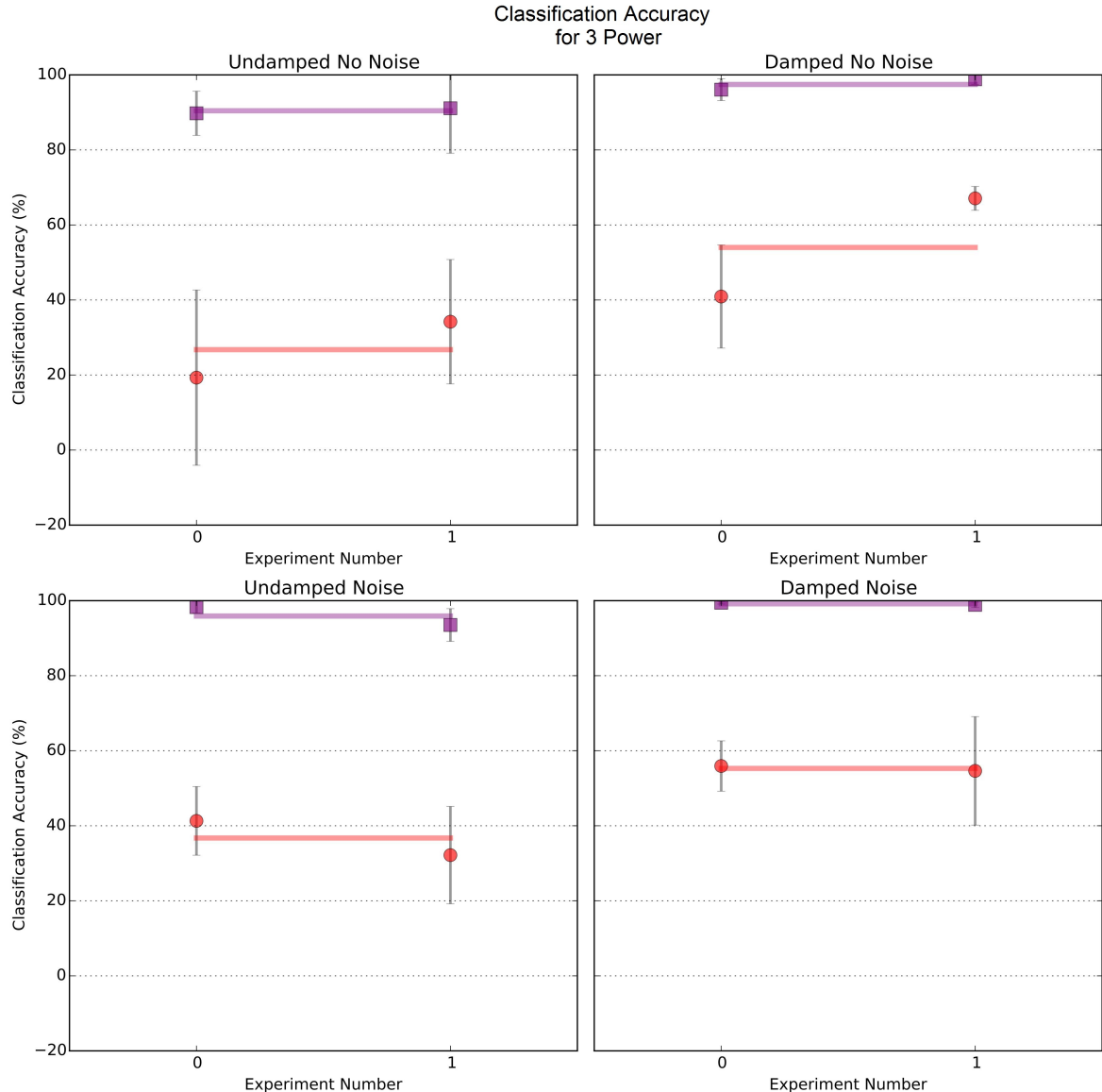


Figure 3.6: This figure shows average (over 3 trials) classification accuracy for the 6.6MHz, -3 power setting. Each quadrant shows a different experimental setup. The x -axis enumerates the different experiments. Tables 3.3 and 3.4 show the exact experiments the numbers represent.

50%. One reason to explain such a poor classification is that the machine learning algorithm did not have enough data to train on, which resulted in underfitting. However, because there were 1440 training points per experiment we suspect that these results are due to the lack of features that are physically correlated with modulus (in contrast to the scatterers which have many features that are physically correlated with scatterer size, as discussed previously).

Changing the ultrasound probe frequency to 10MHz worsened the classification accuracy

by approximately 8% for the induced noise case. However, the change is not significant because changes lie within the range of the uncertainty bars. Accuracy remained similar for the non-noise case. Changing the power setting to -3 had little effect on the classification accuracy of the scatterer phantoms.

3.4.3 Test of Significance

There needs to be a way to test the quality of the SVM classification results. Theoretically, within a given experiment, every trial should produce the same features (the only difference between trials is a small adjustment of the location of the ultrasound probe on the phantom). Therefore, the classification accuracy during each of the five stages of the SVM algorithm (leave-one-out cross-validation) should be the same. Hence, it makes sense to define the SVM results to be of low quality if the classification accuracy varies greatly between the trials.

We performed a χ^2 -test on the five trials for each experiment, using the trial-average classification accuracy as the expected value. There are $5 - 1 = 4$ degrees of freedom. The results are in Figure 3.7.

	Damped Noise		Undamped Noise		
	80Hz	100Hz	80Hz	100Hz	
15kPa vs 35kPa	45.483	26.424	15kPa vs 35kPa	4.169	18.548
7um vs 30um	1.315	0.013	7um vs 30um	0.124	2.375

	Damped No Noise			Undamped No Noise			
	4 cm	5 cm	6 cm	4 cm	5 cm	6 cm	
15kPa vs 35kPa	31.705	17.386	3.183	15kPa vs 35kPa	13.244	9.187	17.18
5kPa vs 35kPa	14.555	12.205	8.831	5kPa vs 35kPa	55.22	14.095	11.713
5kPa vs 15kPa	11.975	23.319	21.038	5kPa vs 15kPa	41.027	19.163	6.601
7um vs 30um	0.094	0.249	0.42	7um vs 30um	1.848	2.22	6.716

Figure 3.7: This table shows the results of the chi-squared test scores performed on each experiment. Green cells are experiments that passed the 95% confidence test. The classification accuracy reported for these experiments are likely to be significant. Red cells are experiments that failed the 95% confidence test. The classification accuracy for these experiments should be called into question. For the top two tables, the frequency refers to the frequency of the induced noise. For the bottom two tables, the length measurement is the ultrasound focus depth. The "7um vs 30um" label is short for the 7-10 μm phantom versus the 30-50 μm phantom.

Here is some motivation for using the trial-average classification accuracy as the expected value in the χ^2 -test. We hypothesize that each experiment has a true mean classification accuracy. Each trial's accuracy is a point chosen from a distribution centered at the true mean classification accuracy. We wish to measure the probability that the accuracy of each trial came from the true distribution. Unfortunately, we do not know the true mean classification accuracy. We could replace true accuracy with the sample mean. However, such a model would be overly optimistic and report a

higher probability that the points were drawn from a single distribution, than the true model would. Therefore, if our model concludes that the accuracy of each trial was not drawn from a single distribution, then the true model would make the same conclusion. On the other hand, if our model concludes that the points were all drawn from a single distribution, the true model is not guaranteed to do the same. If we're only concerned with the first case (trials were not drawn from the same distribution) then the optimistic model is appropriate.

Looking at Figure 3.7 we see that only $\frac{5}{22}$ of the elasticity phantom experiments passed the χ^2 -test. On the other hand, *all* of the scatterer phantom experiments passed the test. While we can say with confidence what the classification accuracy is for the scatterer phantom case, the accuracy for the elasticity experiments are uncertain.

This result agrees well with our previous results thus far. We have established that none of the features defined in Section 3.1 have a direct physical correlation with the modulus of elasticity of the phantoms – so the classification is uncertain. The opposite is true for the scatterer size phantoms.

3.4.4 Different Kernels of the SVM

As mentioned at the start of this section, the SVM algorithm by default uses a Gaussian kernel for classification. A visualization of the Gaussian kernel is shown in Figure 3.8. While

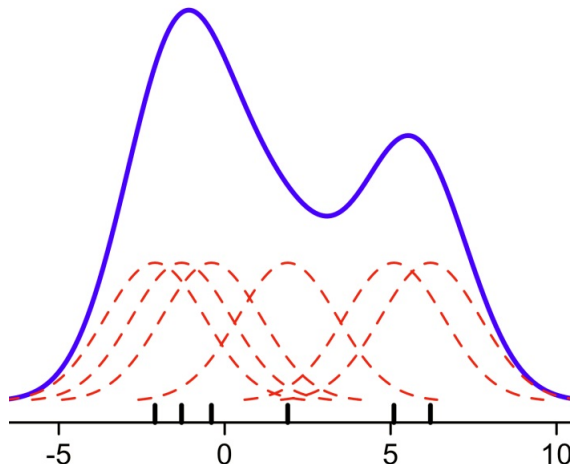


Figure 3.8: This figure shows a Gaussian kernel in 1-Dimensional feature space. The x -axis is the value of the first and only feature. The dotted red lines are the Gaussian kernels centered about one data point each. Each kernel is multiplied by some weight and the total contribution from each kernel is used to model the data. Image courtesy of: https://en.wikipedia.org/wiki/Kernel_density_estimation.

Gaussian kernels are known to work well for SVM classification, many other kernels are possible.

We investigated the use of Linear, Polynomial (of order 3) and Sigmoid kernels.

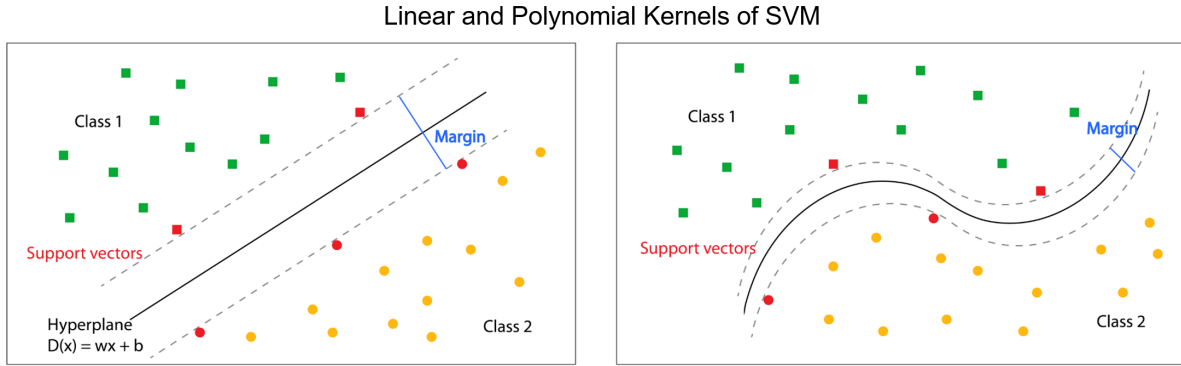


Figure 3.9: A Linear SVM kernel is shown on the left while a Polynomial SVM kernel is shown on the right. The x and y -axis here are the two features in a two-feature classification problem. The SVM algorithm tries to learn a model (shown by the black line) that separates the two classes (green squares and yellow circles) in feature space. For more than 2-dimensions, the separation boundary is a hyper-plane for the Linear kernel and a n^{th} degree polynomial in the polynomial case. Image courtesy of: http://141.61.102.17/perseus_doku/doku.php?id=perseus:activities:matrixprocessing:learning:classificationfeatureselection.

Classification Accuracy with Different Kernels: Elasticity Phantoms

	Undamped No Noise	Damped No Noise	Undamped Noise	Damped Noise
Gaussian	73	71	62	80
Linear	73 [0]	70 [-1]	62 [0]	80 [0]
Polynomial (Degree 3)	68 [-5]	64 [-7]	60 [-2]	80 [0]
Sigmoid	73 [0]	67 [-4]	57 [-5]	78 [-2]

Figure 3.10: This figure shows the SVM classification accuracy using different data kernels for the case of elasticity phantoms. We see very little difference between each of the kernels. The Gaussian kernel was used as a baseline and relative accuracy is shown in square brackets in the cells.

While the Gaussian kernel had the highest accuracy, changing the kernel type does not affect the classification accuracy a lot. In fact, the Linear kernel performed almost as well as the Gaussian kernel. Looking at 3.10 and 3.11, we see that the Polynomial model does worse than the other kernels. This may be surprising at first because the Linear kernel is a "sub-kernel" of the Polynomial kernel in the sense that any model described by the Linear kernel can also

Classification Accuracy with Different Kernels: Scatterer Size Phantoms

	<u>Undamped</u> No Noise	Damped No Noise	<u>Undamped</u> Noise	Damped Noise
Gaussian	87	97	97	96
Linear	87 [0]	96 [-1]	97 [0]	94 [-2]
Polynomial	87 [0]	94 [-3]	97 [0]	95 [-1]
Sigmoid	87 [0]	97 [0]	96 [-1]	97 [+1]

Figure 3.11: This figure shows the SVM classification accuracy using different data kernels for the case of scatterer phantoms. We see very little difference between each of the kernels. The Gaussian kernel was used as a baseline and relative accuracy is shown in square brackets in the cells.

be described by the Polynomial kernel. Therefore, one would expect the Polynomial kernel to do as well as the Linear one, maybe even better. This inconsistency can be explained by the fact that the Polynomial model is over-fitting. During leave-one-out cross-validation, the SVM is over-fitting on the eight training files. It is picking out extraneous patterns that differentiate phantom type I from phantom type II. These patterns are extraneous in the sense they arise from noise and do not represent actual differences between the phantoms. During the validation step when the SVM tests the model on the remaining two data files, the extraneous patterns that the model picked out makes false conclusion about the class the data points belong to.

In short, a hyper-plane is sufficient to differentiate between classes, and any model with higher complexity **will not do better** than the hyper-plane (Linear Model). In fact, we quickly start to over-fit when we increase the Polynomial kernel's degree even by a little bit. This is strong evidence that the classes are linearly separated in feature-space. In fact, this is exactly what we see when we plot the features in feature-space. In Section 3.4.7 we see that the features that have the most classification power: features 1–4 (see Fig. 3.12) form a linear structure, with a linear decision boundary (pick a point in space, and draw a line to separate the classes).

3.4.5 SVM Parameter Grid Search

SVM models could be sensitive to choice of hyper-parameters. In our model, there are two important hyper parameters: C which is proportional to λ (in Eq. 3.13) and describes the severity of regularization in the loss function and γ which is related to the variance of the Gaussian kernel. The Gaussian kernel matrix is defined as,

$$\phi_{ij} = e^{\frac{-(x^i - x^j)^2}{2\sigma^2}}. \quad (3.16)$$

γ is proportional to σ in the kernel equation. We conducted a grid search in hyper-parameter space to look for values of C and γ that gave the best classification accuracy. It turned out the classification accuracy was not sensitive to choice of hyper-parameters. We tried $5 \times 5 = 25$ different combinations of C and γ values. C ranged from 3^{-2} to 3^2 and γ ranged from 3^{-4} to 3^0 , each parameter incremented by multiples of 3. Changing the hyper-parameters caused very little difference in classification accuracy. For the values of C and γ we investigated, average accuracy changed at most 5% from the best to worst case. We found that $C = 1$ and $\gamma = 1/9$ had the best classification accuracy. These are the values we used for classification throughout the report.

3.4.6 Feature Dropout Analysis

To better understand our results, we investigated the effectiveness of subsets of features in classification. We "dropped out" some features and repeated the classification using the Gaussian kernel (which is default for LIBSVM, the SVM library we are using). The results are shown in Figures 3.12, 3.13, 3.14 and 3.15.

Conclusions from Figure 3.12:

- Features 1 – 4 provide near baseline accuracy for both damped cases and the undamped noise case (columns 2 – 4 in Figure 3.12).
- Features 1 – 4 and 5 – 6 are redundant. Row 5 only classified with features 5 – 6 while row 6 only classified with features 1 – 4. They had almost identical accuracy. In addition, rows 3 and 4 did not classify with features 1 – 6 and had much lower accuracy than any row which used either features 1 – 4 or 5 – 6. Comparing rows 2 and 8, we see having either features 1 – 4 or features 5 – 6 guarantees good accuracy. Row 7 implies baseline accuracy can be achieved even if features 5 – 6 can be omitted but if 1 – 4 are used.
- Features 7, 8, and 9 are crucial to the classification of the undamped, no noise case. Rows 5, 6 and 9 did not use any of the features 7, 8 and 9 and had about 10% lower classification accuracy for undamped, no noise.

Conclusions from Figure 3.13:

- Near baseline accuracy for the damped and the undamped no noise cases (columns 2–4 in Figure 3.13) can be achieved using only one of features 1–5.
- Feature 5 is redundant with features 1–4.
- Feature 6 provides little additional information.

Classification Accuracy with Dropout: Scatter Size Phantoms									Undamped No Noise	Damped No Noise	Undamped Noise	Damped Noise	
F1	F2	F3	F4	F5	F6	F7	F8	F9					
									87	97	97	96	
									88 [+1]	96 [-1]	96 [-1]	94 [-2]	
									86 [-1]	73 [-24]	88 [-9]	80 [-16]	
									84 [-3]	81 [-16]	93 [-4]	67 [-29]	
									76 [-11]	96 [-1]	96 [-1]	95 [-1]	
									77 [-10]	96 [-1]	96 [-1]	96 [0]	
									87 [0]	97 [0]	97 [0]	96 [0]	
									79 [-8]	97 [0]	97 [0]	95 [-1]	
									77 [-10]	97 [0]	97 [0]	96 [0]	

Figure 3.12: This table shows the classification accuracy on scatterer phantoms using different combinations of features. **F₁** to **F₉** label the features one to nine defined earlier in the chapter. Each row of the table is one classification with a different set of features. Green cells indicate that feature was used in the classification while gray cells means the feature was omitted. Classification accuracy for the four experimental setups are shown on the right with nine-feature classification as baseline. Relatively accuracy to the baseline are shown in square brackets.

- Feature 9 provides the most consistent accuracy out of all the features across the 4 experimental setups.

Classification Accuracy with One Feature: Scatter Size Phantoms									Undamped No Noise	Damped No Noise	Undamped Noise	Damped Noise	
F1	F2	F3	F4	F5	F6	F7	F8	F9					
									87	97	97	96	
									76 [-11]	97 [0]	96 [-1]	96 [0]	
									76 [-11]	96 [-1]	97 [0]	95 [-1]	
									76 [-11]	96 [-1]	96 [-1]	96 [0]	
									76 [-11]	97 [0]	96 [-1]	96 [0]	
									76 [-11]	96 [-1]	96 [-1]	96 [0]	
									77 [-10]	64 [-33]	83 [-14]	77 [-19]	
									84 [-3]	81 [-16]	93 [-4]	67 [-29]	
									74 [-13]	51 [-46]	79 [-18]	54 [-42]	
									81 [-6]	79 [-18]	84 [-13]	82 [-14]	

Figure 3.13: This table shows the classification accuracy on scatterer phantoms using single features. Green cells indicate that feature was used in the classification while gray cells means the feature was omitted. The nine-feature classification is shown as the baseline. Relatively accuracy to the baseline are shown in square brackets.

Figure 3.14 and 3.15 tell quite a different story for elasticity phantoms:

- While the classification for scatterer phantoms was dominated by some of the features, the classification for elasticity phantoms improves the more features are used. This is evident

when comparing Figures 3.14 and 3.15. Classification accuracy is much lower with one feature versus a group of features.

- Features 1 – 4 do not provide near baseline accuracy as in the scatterer phantoms case.
- While feature 8 classified very poorly in the scatterer phantoms case, it has one of the highest one-feature classification accuracy in the elasticity case.
- Feature 9 has usually low one-feature classification accuracy.

Classification Accuracy with Dropout: Elasticity Phantoms

F1	F2	F3	F4	F5	F6	F7	F8	F9	Undamped No Noise	Damped No Noise	Undamped Noise	Damped Noise
									73	71	62	80
									71 [-2]	67 [-4]	62 [0]	78 [-2]
									69 [-4]	58 [-13]	60 [-2]	80 [0]
									70 [-3]	53 [-18]	57 [-5]	82 [+2]
									61 [-12]	64 [-7]	62 [0]	74 [-6]
									68 [-5]	73 [+2]	57 [-5]	81 [+1]
									72 [-1]	71 [0]	58 [-4]	81 [+1]
									72 [-1]	71 [0]	62 [0]	80 [0]
									68 [-5]	73 [+2]	61 [-1]	82 [+2]

Figure 3.14: This table shows the classification accuracy on elasticity phantoms using different combinations of features. \mathbf{F}_1 to \mathbf{F}_9 label the features one to nine defined in Section 3.1. Each row of the table is one classification with a different set of features. Green cells indicate that feature was used in the classification while gray cells means the feature was omitted. Classification accuracy for the four experimental setups are shown on the right with nine-feature classification as baseline. Relatively accuracy to the baseline are shown in square brackets.

3.4.7 Feature Visualization

There are two main questions from the results of the previous sections: why is classification accuracy for scatterer phantoms better than elasticity phantoms, and why do features 1 – 4 classify scatterer phantoms so well? In this section, we try to answer these questions by plotting the features in 3-D.

Our analysis begins with the the scatterer phantoms. Features 1 – 3 are plotted in Figure 3.16. Judging from the results of the previous section, Features 1 – 4 all classify equally well. Therefore, we expect the plots to look similar for any 3 choices of the 4 features. This is what we saw, and we decided it was appropriate to only present the plot for features 1 – 3 here.

Classification Accuracy with One Feature: Elasticity Phantoms									Undamped No Noise	Damped No Noise	Undamped Noise	Damped Noise	
F1	F2	F3	F4	F5	F6	F7	F8	F9					
									73	71	62	80	
									58 [-15]	60 [-11]	58 [-4]	64 [-16]	
									67 [-6]	61 [-10]	57 [-5]	75 [-5]	
									59 [-14]	59 [-12]	56 [-6]	72 [-8]	
									62 [-11]	64 [-7]	54 [-8]	69 [-11]	
									62 [-11]	59 [-12]	57 [-5]	69 [-11]	
									57 [-16]	58 [-13]	65 [+3]	75 [-5]	
									70 [-3]	53 [-18]	57 [-5]	82 [+2]	
									68 [-5]	57 [-14]	58 [-4]	80 [0]	
									53 [-20]	49 [-22]	51 [-11]	49 [-31]	

Figure 3.15: This table shows the classification accuracy on elasticity phantoms using single features. Green cells indicate that feature was used in the classification while gray cells means the feature was omitted. The nine-feature classification is shown as the baseline. Relatively accuracy to the baseline are shown in square brackets.

As alluded in Section 3.4.4 (where we investigated the over-fitting of polynomial kernels), we expect the two phantom types to be simply separated in feature space. This is what we see in Figure 3.16. The dots represent the phantom with scatterer size $7 - 10\mu\text{m}$ while the crosses represent the phantoms with scatterer size $30 - 50\mu\text{m}$. The two different phantoms appear to be separable with a hyper-plane. We also observe that while the $7 - 10\mu\text{m}$ phantom lies in a cluster at high values of features 1 – 3, the $30 - 50\mu\text{m}$ phantom is spread out from low to medium values of features 1 – 3. The $\mathbf{F}_1, \mathbf{F}_2, \mathbf{F}_3$ feature space essentially looks like a radial vector co-linear with $(1, 1, 1)$. This implies that the effect is just magnitude scaling; the proportion of individual frequencies is more or less the same between phantom types. Finally, When looking at the $\mathbf{F}_1, \mathbf{F}_2, \mathbf{F}_3$ feature space the experiments on the damped tables have more spread in the $\mathbf{F}_1 - \mathbf{F}_2$ plane than the experiments on the undamped tables.

At this point the reader may be skeptical about how well the two phantom types are separated in feature space. But the results are reproducible. When we make the same 3D plots for the second set of data we acquired (6.6MHz –3 power and 10MHz 0 power experiments), we see the same structures. The $7 - 10\mu\text{m}$ scatterer phantom tends to form a blob higher up in feature space while the $30 - 50\mu\text{m}$ phantom is spread out along a lower part of feature space. Furthermore, if we look at the top two graphs of Figure 3.18, we see that the spread of of the 15kPa and 35kPa phantoms in features 1 – 3 resemble that of the $30 - 50\mu\text{m}$ sample in /refvisual1. This is consistent because the elasticity phantoms have scatterer size of $30 - 50\mu\text{m}$.

Plots of the features 7, 8, 9 for the scatterer experiments are shown in Figure 3.17. We see that when looking at the 9 – 7 plane, all the blue dots ($7 - 10\mu\text{m}$) lie on Fractal Dimension = 2.

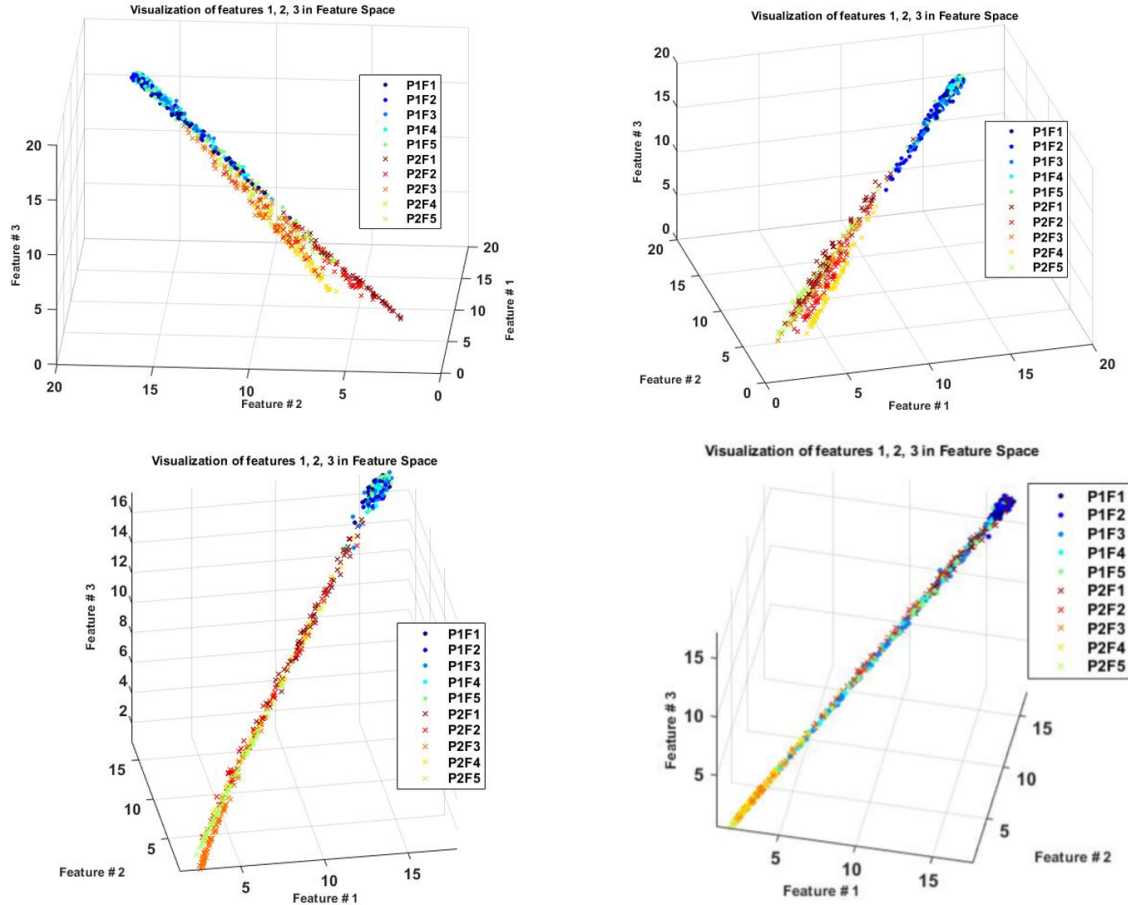


Figure 3.16: Plots of data points in feature space for scatterer phantoms. Features 1, 2, 3 are plotted on the x , y , z axes respectively. Top left: Damped with 80Hz Noise. Top right: Damped No Noise. Bottom left: Undamped 80Hz Noise. Bottom right: Undamped No Noise. The legend indicates the phantom and file numbers. For example, P1F3 means the third trial for phantom I. Phantom I in this case was $7 - 10\mu\text{m}$ while Phantom II was $30 - 50\mu\text{m}$.

But there is a large variance for the red dots ($30 - 50\mu\text{m}$).

Looking at the modulus experiments for the \mathbf{F}_1 , \mathbf{F}_2 , \mathbf{F}_3 space, the spread looks like that of the $30 - 50\mu\text{m}$ sample in the scatterer phantoms. This is consistent since scatterer size for the elasticity phantoms was actually $30 - 50\mu\text{m}$.

Finally, we note that we have omitted features 5 and 6 in our visualization because we showed that they are redundant with features 1 – 4.

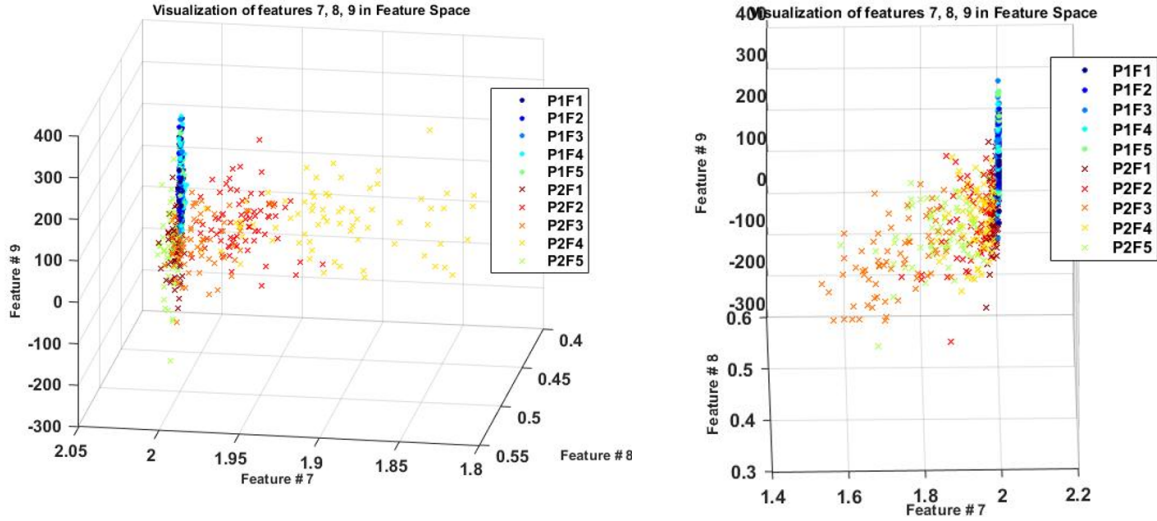


Figure 3.17: Plots of data points in feature space for scatterer phantoms. Features 7, 8, 9 are plotted on the x , y , z axes respectively. Left: Damped No Noise. Right: Undamped 80Hz Noise. The legend indicates the phantom and file numbers. For example P1F3 means the third trial for phantom I. Phantom I in this case was $7 - 10 \mu\text{m}$ while Phantom II was $30 - 50 \mu\text{m}$.

3.4.8 Physical Model and Validation

Based on past ultrasound experiments and theory that can be found in the works of Lizzi et al. 1996 [14], the power spectrum from sample tissue under ultrasound imaging can be expressed as

$$S(f) = 4k^2 \int \int \int R_\zeta(\Delta x) R_D(\Delta y \Delta z) R_G(\Delta x) e^{-j2k\Delta x} d\Delta x \quad (3.17)$$

where R_ζ , R_D , and R_G respectively represent the spatial autocorrelation functions of a tissue's acoustic impedance, two-way beam directivity function, and Hamming window [14]. An autocorrelation function in a time series context is defined as the cross-correlation, or linear dependence, between a function and itself at various points in time. Explicitly, the functions R_ζ is

$$R_\zeta(\Delta x) = K e^{-(\frac{1.17\Delta x}{\alpha})^2 - (\frac{1.17\Delta y}{\beta})^2 - (\frac{1.17\Delta z}{\gamma})^2} \quad (3.18)$$

where α , β , and γ represent the dimensions of the scatterer size in the sample tissue. In the experiments discussed in this report, the scatterers in the sample phantoms are assumed to be spherical, meaning that $\alpha = \beta = \gamma = r$ where r is the radius of a spherical scatterer. K is a parameter defined as:

$$K = V C Q^2. \quad (3.19)$$

where V is the volume of a single scatterer, C is the concentration of scatterers, and Q is a constant related to the acoustic impedance of the sample [14]. For the Philips phantoms provided,

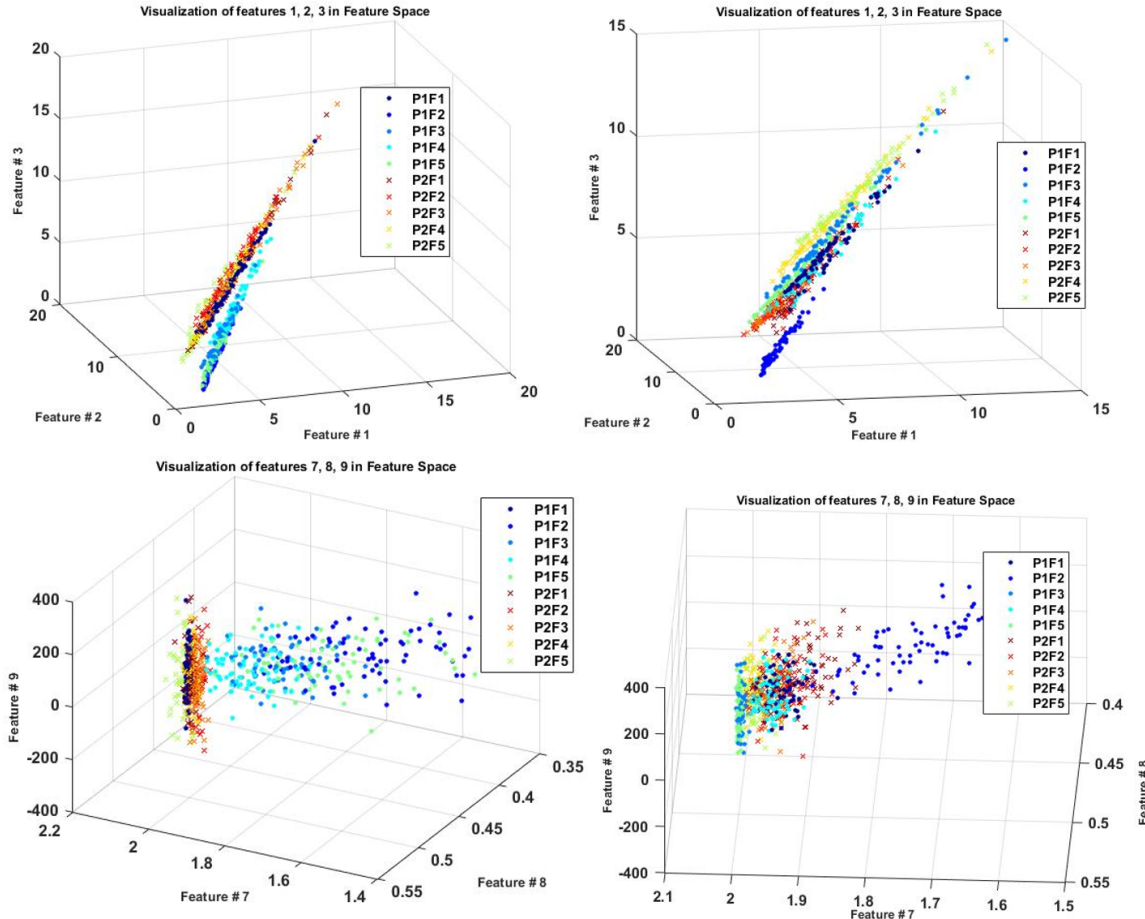


Figure 3.18: Plots of data points in feature space for elasticity phantoms. The top two graphs plot features 1 – 3 while the bottom two graphs plot features 7 – 9. Top left: Damped 80Hz Noise. Top right: Damped No Noise. Bottom left: Damped 80Hz Noise. Bottom right: Damped No Noise. The legend indicates the phantom and file numbers. For example P1F3 means the third trial for phantom I. Phantom I in this case was 15kPa while Phantom II was 35kPa.

the acoustic impedance between regions of the phantom is constant, and because the scatterers are assumed to be spherical, the product of V , which scales with radius³, and C , which scales with 1/radius³ is a constant. As far as our experiments are concerned, K is a constant.

The R_D function is

$$R_D(\Delta r) = \frac{k^2 a^2}{4\pi R^2} \int \int F^2(y, z) F^2(y + \Delta y, z + \Delta z) dy dz \quad (3.20)$$

where k is the wave number, $\frac{2\pi f}{v}$, dependent on the input frequency f and velocity of sound v in the phantom. The function f in this equation is defined as

$$F(y, z) = \frac{2J_1(kar/R)}{kar/R} \quad (3.21)$$

where a is related to the aperture size of the transducer, R is the focal depth of the image, and J_1 is a Bessel function of the first kind and first order [14]. In our experiments, every component in this equation is a constant.

The final component of the power spectrum equation 3.17 is R_G , which can be assumed to be a constant value, $R_G = L$ [14].

By substituting these equations back into the power spectrum equation, Eq. 3.17, one can simplify the expression to:

$$S(f) = \frac{0.4Lk^4(\frac{a}{R})^2K(r^3)e^{-(\frac{kr}{1.17})^2}}{1 + 0.22(\frac{kar}{1.17R})^2} \quad (3.22)$$

A detailed derivation of the equation can be found in the works of Lizzi et al. 1996 [14]. Looking at this form of the power spectrum equation and recalling that a negative exponential decreases faster than a polynomial grows, it can be deduced that for increasing r , or increasing scatterer sizes, the numerator is dominated by the negative exponential term, decreasing the spectral power with increasing r . The denominator has an r^2 term which also contributes to decreasing the spectral power. To visualize the trend clearly, we can say for large r (although unrealistic), the spectral power formula behaves like,

$$S \sim re^{-r^2}, \quad (3.23)$$

which clearly decreases with increasing r . The conclusion to be drawn from this theory is that with **increasing scatterer sizes, the power spectrum decreases**. Because the power spectrum is derived from the Fourier transform and the features described in section 3.1 used for classification are extracted from the Fourier transform, it can be deduced that classification on phantoms with different scatterer sizes has more separation power than on phantoms with varying elastic moduli. This means that frequency dependent features used are more closely related to the scatterer sizes than elastic moduli, a result confirmed in by the work of Kolios and Czarnota 2008 [13].

"It is therefore clear that the nucleus or cell size significantly influences the ultrasound backscatter strength and its frequency dependence... which is consistent with theory."

– Kolios and Czarnota 2008 [13]

This deduction can also be seen in the results presented in the analysis in Section 3.4.7, where the features used with the SVM classified the scatterer phantoms consistently better than the elasticity phantoms.

DENOUEMENT

4.1 Experimental Limitations

As mentioned in Chapter 2, we had no control over the design of the tissue phantoms. Philips stated that the phantoms were homogeneous and either 5kPa, 15kPa or 35kPa in elastic modulus and $7 - 10\mu\text{m}$ or $30 - 50\mu\text{m}$ in scatterer diameter. We are uncertain of the accuracy of these claims. Some of our other concerns include: the phantom division boundary, the size of the phantoms, and the container used to hold the phantoms. The phantoms came in large, rectangular containers with two to three phantom types in each container. The different phantoms in one container were separated from left to right. For example, the 5kPa phantom fills up the left third of the container, the 15kPa fills up the middle third and the 35kPa fills up the right third (refer to Figure 2.3). The only indication of where one phantom ended and where another phantom started is a boundary draw on the front face of the phantom container. We are unsure of the accuracy of these line markings.

The problem with having multiple phantoms in one container is that when the ultrasound waves enter phantom A, some the energy will inevitably travel to the adjacent phantom B. Therefore in any experiment, the ultrasound signal we acquire is not purely the response from the phantom under investigation, there is contribution from adjacent phantoms. We could not simply place the ultrasound probe as far away from the division boundaries as possible because putting the probe too close to the walls of the container would create artifacts in the ultrasound signal. In short, if division boundaries are not accurate then there is a chance we place the ultrasound probe too close to adjacent phantoms in some of our experiments. **In addition, during data acquisition, we probed different parts of the phantom.** It is possible that significant differences in the features between trials were a result of placing the probe too close to the division boundary in some

of the trials. This could help to explain why the elasticity phantoms performed so poorly on the chi-squared test. As seen in Figure 2.3 and 2.4, there are three different phantoms in one container for the elasticity phantoms but only two different phantoms in one container for the scatterer phantoms. Therefore adjacent phantoms would have affected the measurement much more in the elasticity case than in the scatterer case. All of these problems can be mitigated by using phantoms constructed in separate containers.

Another concern we had was the size of the phantoms. We are uncertain whether the optical table had a significant effect on the ultrasound response of the phantom. This is because the container holding the phantom had hard, rigid walls and the phantoms themselves were large and heavy. **Therefore, the optical table may have been poorly coupled to the phantoms.** The reasoning for large phantoms is to reduce the effect of edge effect where the ultrasound energy bounces off the walls of the container. However, in an experiment where we want to investigate the effects of damping on an optical table, this is disadvantageous. Ideally, the phantom would be held in a wide, long but shallow container so as to minimize edge effects but still allow the optical table to play a role. This is a consideration for future experiments.

Because the phantoms came in large, heavy containers, we were limited with the optical tables we could have used. Many of the optical tables available to the lab were unable to support the weight of the phantoms. We used an optical table in one of the labs in an adjacent building. The lab had other machinery operating and was particularly noisy. But because the optical table itself had to be large to hold the phantom, we could not move it to a different room. The noisiness of the room in which we conducted the experiment could have adversely affected the signal of the ultrasound.

The ultrasound machine we used was the Analogic SonixTouch. **However, we initially intended to use the Philips IU22 machine.** Due to unexpected delays from Philips, the DAQ board for the Philips machine did not arrive. The Philips machine is known to have better ultrasound resolution and produces higher quality data than the Analogic machine. Therefore, the results of our experiments could be improved by using the Philips machine in the future.

The Analogic machine comes with its own data acquisition software. However, to make the data acquisition more efficient, we used third party software that interfaced with the native Analogic software. During experimentation, we noticed that the third party software contained bugs and crashed from time to time. Therefore, the quality of our data could have been compromised by the software that we used.

Finally, some of the MATLAB files we used to extract features came from our sponsors. While

we had written scripts ourselves for feature extraction, the sponsor insisted on using their scripts in order to guarantee the behavior is consistent with their previous results. While we reviewed the sponsor's code to the best of our ability, it is possible that undesirable behavior in the code could introduce artifacts into the features. These artifacts could in turn cause artificially high classification accuracy. Because of time constraints, we did not repeat the analysis with features extracted from our own MATLAB scripts. This is a logical next step for future work and a good test to see whether the results are reproducible.

4.2 Conclusions

The primary results of this project are as follows:

- For elasticity phantoms the no noise case, mean classification accuracy is approximately the same with (71%) and without the optical table (72%). For the induced noise case, accuracy was damped (80%) and undamped (62%) case. However, many experiments failed χ^2 -test and are not statistically significant.
- For scatterer phantoms the mean classification accuracy was between 87% – 97% with small variance between trials. All experiments passed χ^2 -test and are statistically significant.
- Noise can improve classification accuracy for scatterer phantoms **only** in the case of undamped with noise added – but this agrees with theory.
- We were not able to reproduce the results of previous studies. We found no significant change in classification accuracy on **optimal** table. From this results we conclude that microvibrations from external noise are not a reliable source of information in RTFS classification.
- Changing the ultrasound probe frequency to 10MHz worsened the classification accuracy by approximately 8% for the induced noise case. However, the change is not significant because changes lie within the range of the uncertainty bars.
- Changing the ultrasound probe power setting to -3 had little effect on the classification accuracy of the scatterer phantoms.
- While the Gaussian kernel had the highest accuracy, changing the kernel type did not affect the classification accuracy by any considerable margin. In fact, the Linear kernel performed almost as well as the Gaussian kernel. Better features may need to be chosen to capture complexity in the ultrasound data.
- Features 1 – 4 and 5 – 6 are redundant. Classification is just as good without using features 5 – 6.

- Features 1 – 4 caused the high scatterer phantom classification accuracy, but they do not perform well for the elasticity phantoms. In that case, every feature is required for acceptable classification accuracy.
- The two different scatterer phantoms can be easily separated in feature space. While the $7 - 10\mu\text{m}$ phantom lies in a cluster at high values of features 1 – 3, the $30 - 50\mu\text{m}$ phantom is spread out from low to medium values of features 1 – 3.
- The Fourier transform features are more dependent on scatterer size than elastic modulus.

CHAPTER



PROJECT DELIVERABLES

5.1 List of Deliverables

The deliverables for the investigation are as follows:

- Report of experimental results
- MATLAB scripts used for data analysis
- Raw data of performed experiments

We have written a report with experiments conducted as well as our analysis of the results. In addition, we have produced a small MATLAB script package containing all of the files we used in data feature extraction, data cleansing, and classification using a SVM. At this time, our sponsors have not decided whether the results of the project should be formulated into an academic paper for publish. The scope of the project changed from our initial proposal to exclude simulations as discussed in Section 1.5.

5.2 Financial Summary

All of the equipment and lab space was provided by the sponsors of the project. We were given access to all of the ultrasound equipment in Kaiser 3080 and 3090 on the campus of the University of British Columbia. Our project did not require the use of any additional funds, so there is no financial summary to report.

5.3 Ongoing Commitments

The sponsor has requested for us to acquire more data to characterize the phantoms in more detail. The scheduled date for us to perform these experiments is April 7th 2016.

CHAPTER



RECOMMENDATIONS

In this section a short list of recommended steps in the future will be provided along with an explanation of why the action is suggested, how it should be done, and what the outcome should be.

1. As discussed in the denouement section, the phantoms we used were potentially too large to accurately test on an optical table. The optical table's damping function **falls with distance**, so a large phantom sample may not experience much damping near the sample region at the top. Also the presence of multiple regions in one phantom block may have affected the data. To minimize these effects and reproduce the results seen in these experiments, similar trials could be run but with smaller phantoms individually isolated for different elastic moduli or scatterer size. More phantoms of different parameters could also be tested on to verify the conclusions in Section 4.2.
2. Investigate the ultrasound response of phantoms with different viscous properties. As mentioned in the introduction, human tissue is a viscoelastic material with both elastic and viscous properties. Therefore, it is insufficient to only investigate the effect of changing the elastic modulus. Changing the viscous properties could introduce structures to the ultrasound signal that will lead to more accurate classification. We are not in a position to consult on the construction of such phantoms. Instead it is recommended that the sponsor consults Philips.
3. Investigate possible new features to use in classification. The nine features used in the current SVM model is dependent on the scatterer size of the sample, as confirmed by the theory in Section 3.4.8. To classify between tissues with various elastic properties, different features, such as features more related to absorption could be utilized.

4. Try Other Machine Learning Models Given the clear separation of the phantoms in feature space, Generative models such as Gaussian mixture models may perform well on classification. Matlab libraries for other machine learning techniques are available online. Another problem with SVM classification is that it may not work well across different tissue samples. For example, a model could be trained on patient A but the model may test poorly on patient B. A hybrid model may be possible in which information is gathered about the physical properties of a specific patient's tissue. This information could be used to augment the SVM model.

BIBLIOGRAPHY

- [1] M. ALI, D. MAGEE, AND U. DASGUPTA, *Signal processing overview of ultrasound systems for medical imaging*, SPRAB12, Texas . . . , (2008), pp. 1–27.
- [2] S. ARIVAZHAGAN AND L. GANESAN, *Texture classification using wavelet transform*, 24 (2003), pp. 1513–1521.
- [3] C.-C. CHANG AND C.-J. LIN, *LIBSVM : A Library for Support Vector Machines*, (2013), pp. 1–39.
- [4] R. CHOU, J. M. CROSWELL, T. DANA, C. BOUGATSOS, I. BLAZINA, AND R. FU, *Review Annals of Internal Medicine Screening for Prostate Cancer : A Review of the Evidence for the*, Ann Intern Med, 155 (2011), pp. 762–771.
- [5] M. I. DAOUD, P. MOUSAVI, F. IMANI, R. ROHLING, AND P. ABOLMAESUMI, *Tissue classification using ultrasound-induced variations in acoustic backscattering features.*, IEEE transactions on bio-medical engineering, 60 (2013), pp. 310–320.
- [6] S. M. FALZARANO AND C. MAGI-GALLUZZI, *Staging prostate cancer and its relationship to prognosis*, Diagnostic Histopathology, 16 (2010), pp. 432–438.
- [7] E. J. FELEPPA, C. R. PORTER, J. KETTERLING, P. LEE, S. URBAN, AND A. KALISZ, *and Monitoring Treatment of Prostate Cancer*, 26 (2006), pp. 163–172.
- [8] S. M. HAN, H. J. LEE, AND J. Y. CHOI, *Computer-aided Prostate Cancer Detection using Texture Features and Clinical Features in Ultrasound Image*, Journal of Digital Imaging, 21 (2008), pp. 121–133.
- [9] A. C. HODGE, A. FENSTER, D. B. DOWNEY, AND H. M. LADAK, *Prostate boundary segmentation from ultrasound images using 2D active shape models: Optimisation and extension to 3D*, Computer Methods and Programs in Biomedicine, 84 (2006), pp. 99–113.
- [10] F. IMANI, *Ultrasound-based Tissue Typing Using RF Time Series : Clinical Feasibility Studies and Applications*, PhD thesis, Queen’s University, 2014.
- [11] F. IMANI, B. ZHUANG, A. TAHMASEBI, J. T. KWAK, S. XU, H. AGARWAL, S. BHARAT, N. UNIYAL, I. B. TURKBEY, P. CHOYKE, P. PINTO, B. WOOD, M. MORADI, P. MOUSAVI,

- AND P. ABOLMAESUMI, *Augmenting MRI- $\ddot{\text{a}}$ transrectal ultrasound-guided prostate biopsy with temporal ultrasound data: a clinical feasibility study*, International Journal of Computer Assisted Radiology and Surgery, 10 (2015), pp. 727–735.
- [12] M. INAHARA, H. SUZUKI, H. NAKAMACHI, N. KAMIYA, M. SHIMBO, A. KOMIYA, T. UEDA, T. ICHIKAWA, K. AKAKURA, AND H. ITO, *Clinical evaluation of transrectal power doppler imaging in the detection of prostate cancer*, International urology and nephrology, 36 (2004), pp. 175–180.
- [13] M. C. KOLIOS AND G. J. CZARNOTA, *High frequency ultrasound scattering from mixtures of two different cells lines : tissue characterization insights*, pp. 23–25.
- [14] F. L. LIZZI, M. ASTOR, A. KALISZ, T. LIU, D. J. COLEMAN, R. SILVERMAN, R. URSEA, AND M. RONDEAU, *Ultrasonic Spectrum Analysis for Assays of Different Scatterer Morphologies : Theory and Very-High Frequency Clinical Results*, (1996), pp. 1155–1159.
- [15] R. LLOBET, J. C. PEREZ-CORTES, A. H. TOSELLI, AND A. JUAN, *Computer-aided detection of prostate cancer*, International Journal of Medical Informatics, 76 (2007), pp. 547–556.
- [16] U. MANUAL, *SonixMDP/SP/OP Q+ Ultrasound System*.
- [17] M. MORADI, P. ABOLMAESUMI, AND P. MOUSAVI, *Tissue typing using ultrasound RF time series: experiments with animal tissue samples.*, Medical Physics, 37 (2010), pp. 4401–4413.
- [18] M. MORADI, S. MEMBER, P. ABOLMAESUMI, D. R. SIEMENS, E. E. SAUERBREI, A. H. BOAG, P. MOUSAVI, AND S. MEMBER, *Augmenting Detection of Prostate Cancer in Transrectal Ultrasound Images Using SVM and RF Time Series*, 56 (2009), pp. 2214–2224.
- [19] N. M. TOLE, *Interaction of Ultrasound with Matter*, 2005.
- [20] N. M. TOLE, *Ultrasound beam shape.pdf*, 2005.
- [21] P.-H. TSUI AND C.-C. CHANG, *Imaging local scatterer concentrations by the Nakagami statistical model.*, Ultrasound in medicine & biology, 33 (2007), pp. 608–619.
- [22] M. ZHANG, P. NIGWEKAR, B. CASTANEDA, K. HOYT, J. V. JOSEPH, A. DI SANT'AGNESE, E. M. MESSING, J. G. STRANG, D. J. RUBENS, AND K. J. PARKER, *Quantitative Characterization of Viscoelastic Properties of Human Prostate Correlated with Histology*, Ultrasound in Medicine & Biology, 34 (2008), pp. 1033–1042.